CFD Benchmark Tests for Indoor Environmental Problems: Part 4 Air-Conditioning Airflows, Residential Kitchen Airflows and Fire-Induced Flow

Kazuhide Ito*, Kiao Inthavong, Takashi Kurabuchi, Toshikatsu Ueda, Tomoyuki Endo, Toshiaki Omori, Hiroki Ono, Shinsuke Kato, Koji Sakai, Yoshihide Suwa, Hiroshi Matsumoto, Hajime Yoshino, Weirong Zhang and Jiyuan Tu

Interdisciplinary Graduate School of Engineering Science, Kyushu University, 6-1 Kasuga-koen, Kasuga, Fukuoka, 816-8580 Japan

Abstract: Computational Fluid Dynamics (CFD) has become practical design tool for indoor environment recent years and the application cases have been increasing. Though the improvement of the prediction accuracy of CFD is needed in connection with the upgrade of design quality in indoor environment and Heating, Ventilation and air-conditioning (HVAC) system, the prediction accuracy of CFD simulation depends on the understanding for the fundamentals of fluid dynamics and the setting of appropriate boundary and numerical conditions as well. Additionally, deeper understanding to a specific problem regarding indoor environment is also required. The series of this study aimed to provide with the practical information such as prediction accuracy and problematic areas related to CFD applications in air conditioning and ventilation, then performed benchmark tests and reported the results. Especially in this Part 4, benchmark test results for Air-conditioning airflows, Residential kitchen airflows and Fire-induced flow were introduced and discussed.

Keywords: Indoor environment, Computational Fluid Dynamics, Benchmark test, Air-conditioning airflows, Residential kitchen airflows, Fire-induced flow.

1. INTRODUCTION

Commercially available Computational Fluid Dynamics (CFD) software is practically applied in indoor environmental design recent years but the prediction accuracy of CFD simulation depends on the understanding for the fundamentals of fluid dynamics and the setting of appropriate boundary and numerical conditions as well. Additionally, deeper understanding to a specific problem regarding indoor environment is also requested.

This study series is treated as benchmark tests of CFD simulations associated with indoor environmental problems and consist of four parts. The previous three papers reported benchmark test results concerning (1) Isothermal 2-D/3-D airflows, (2) Non-isothermal 2-D/3-D airflows, [1]; (3) Cross-ventilation airflows, (4) Floor heating (panel) systems, [2] and (5) Numerical thermal manikins [3]. In this paper (Part 4), benchmark test results for (6) Air-conditioning airflows, (7) Residential kitchen airflows, (8) Fire-induced flow, are introduced.

2. BENCHMARK TEST FOR INDOOR AIR-CONDITIONING AIRFLOWS

Indoor thermal flows are influenced by natural convection generated by perimeter loads in the building through heat transfer from solar radiation through walls and glass windows; internal heat loads through lighting, human bodies, and office automation (OA) instruments; and by forced convection generated by air conditioners. To predict the flow and temperature fields in the air-conditioned room using CFD, airflow supplied from a complex-shaped diffuser (such as an Anemostat-type) must be reproduced. The capacity of a computer is still insufficient to reproduce the detail geometry of the diffuser faithfully for analyzing the entire room. Thus, to address this issue, some simplifications/modeling are required. In this section, assuming that a personal computer was used to perform a CFD analysis of indoor airflows, special attention was paid to the reproducibility of diffused airflows in rooms with cooling condition. Here, we also introduce (1) a method for setting the boundary conditions for an Anemostat type air diffuser that possesses enough accuracy to be applied practically (for use in practical HVAC design, applied research, etc.) while using the minimum mesh number, and (2) the mesh dependence for cases where the a circular Anemostat-type air diffuser was applied.

2.1. Anemostat-Type Air Diffuser Boundary Conditions

For an anemostat-type air diffuser, we chose the boundary conditions reported by Momoi, *et al*. [4]. A detailed experiment was carried out where the air velocity distribution was measured at 400 mm away

*Address correspondence to this author at the Interdisciplinary Graduate School of Engineering Science, Kyushu University, 6-1 Kasuga-koen, Kasuga, Fukuoka, 816-8580 Japan; Tel: +81 92 583 7628; Fax: +81 92 583 7627; Email: ito@kyudai.jp

E-ISSN: 2409-9821/15

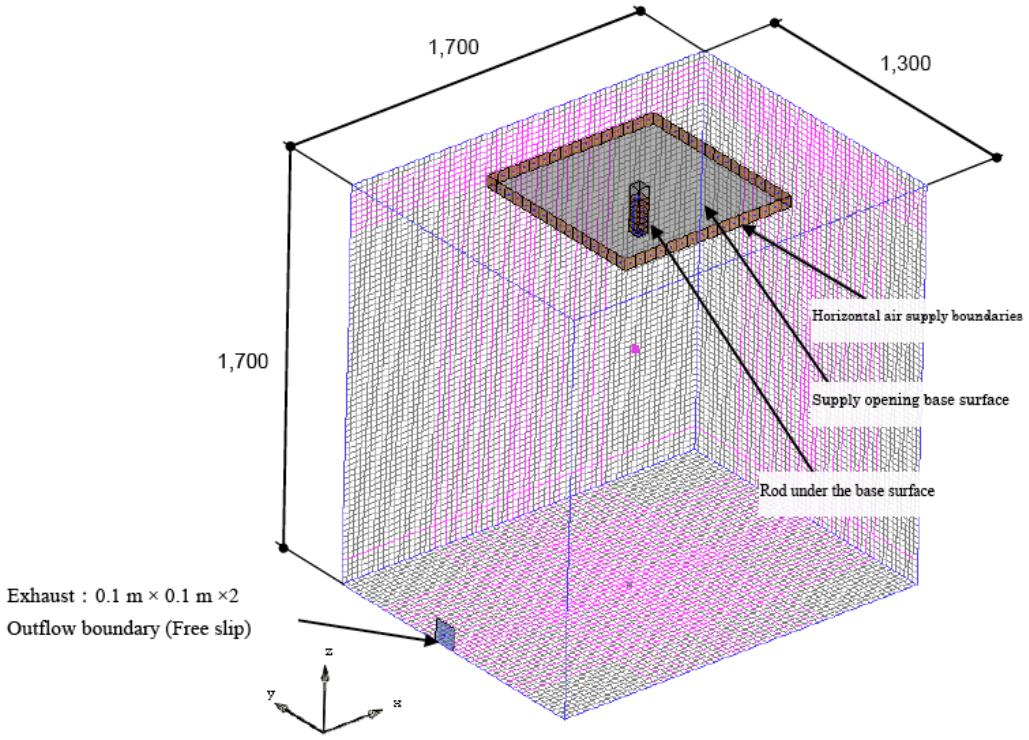

Figure 1: Anemostat-type supply opening boundaries and target of analysis.

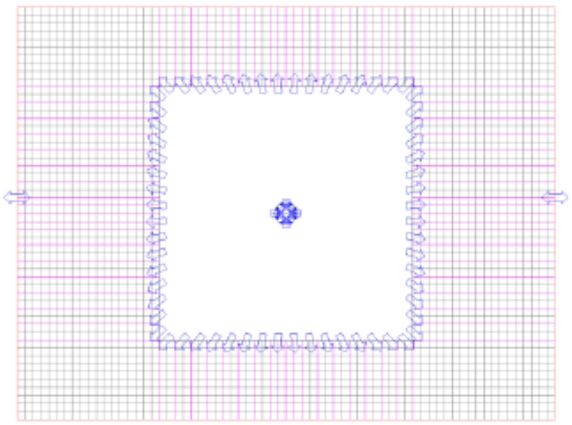

Figure 2: Mesh design of the diffusion boundaries (diffusion boundary – 32 elements).

from the diffuser. Then boundary conditions were created assuming that the circumference (with 800 mm for each side) around the air diffuser was used as a virtually diffused surface. Figure **1** shows the air diffuser shape and in CFD replicating the experiment [4]. This method applies rod-shaped boundary conditions directly below the air diffuser to (1) reproduce the supplied airflow coming down from the center, flowing directly below it, (2) apply horizontally diffused airflow components to side surfaces, and (3) apply induced airflow components to the base surface. Figure **2** shows the mesh design of the area around the air diffuser. The boundary surface was discretized into 32 segments (meshes) and assigned blowing conditions for each discretized segment. Tables **1-3** summarises the boundary conditions on the air diffuser surfaces.

A CFD analysis was performed in accordance with the experimental scenario using the commercial CFD code CRADLE/STREAM (Code-C, see Note). The standard k-ε model was used along with SIMPLEC for the pressure-velocity coupling, and QUICK for the discretization scheme. The CFD analysis reported in Momoi *et al*. [4] used the following settings: the standard k-ε model for turbulence, SMAC for the pressure-velocity coupling, and QUICK for the discretization scheme. Figure **3** shows the comparisons

Table 1: Boundary conditions for Horizontal Diffusion

No.	Normal Component [m/s]	Tangential Component [m/s]	V [m/s]	k [m^2/s^2]	ε [m^2/s^3]	A [m^2]	No. of Locations	Flow rate	
								[m^3/h/1 Location]	Total [m^3/h]
1	1.200	0.076	1.202	0.0517080	0.0152130	0.0025	8	10.8	86.4
2	1.164	0.219	1.184	0.0517080	0.0152130	0.0025	8	10.5	83.8
3	1.098	0.344	1.151	0.0517080	0.0152130	0.0025	8	9.9	79.1
4	1.012	0.443	1.105	0.0517080	0.0152130	0.0025	8	9.1	72.9
5	0.916	0.516	1.051	0.0517080	0.0152130	0.0025	8	8.2	66.0
6	0.819	0.563	0.994	0.0517080	0.0152130	0.0025	8	7.4	59.0
7	0.727	0.591	0.937	0.0517080	0.0152130	0.0025	8	6.5	52.3
8	0.642	0.602	0.880	0.0517080	0.0152130	0.0025	8	5.8	46.2

Table 2: Induced Airflow Boundaries

No.	Normal Component [m/s]	Tangential Component [m/s]	V [m/s]	k [m^2/s^2]	ε [m^2/s^3]	A [m^2]	No. of Locations	Flow rate	
								[m^3/h/1 Location]	Total [m^3/h]
16	0.203144	0.000	0.203144	0.000412676	1.72189E-06	0.6375	1	466.2	86.4

Table 3: Diffusion conditions for Downward Diffusion

No.	Normal Component [m/s]	Tangential Component [m/s]	V [m/s]	k [m^2/s^2]	ε [m^2/s^3]	A [m^2]	No. of Locations	Flow rate	
								[m^3/h/1 Location]	Total [m^3/h]
9	-0.200	0.000	0.200	0.0517080	0.0152130	0.0013	4	-0.9	-3.6
10	-0.200	0.000	0.200	0.0517080	0.0152130	0.0013	4	-0.9	-3.6
11	0.000	0.600	0.600	0.0517080	0.0152130	0.0013	4	0.0	0.0
12	0.300	1.100	1.140	0.0517080	0.0152130	0.0013	4	1.4	5.4
13	0.150	1.200	1.209	0.0517080	0.0152130	0.0013	4	0.7	2.7
14	0.200	0.700	0.728	0.0517080	0.0152130	0.0013	4	0.9	3.6
15	1.600	0.300	1.628	0.0517080	0.0152130	0.0013	4	3.6	14.4

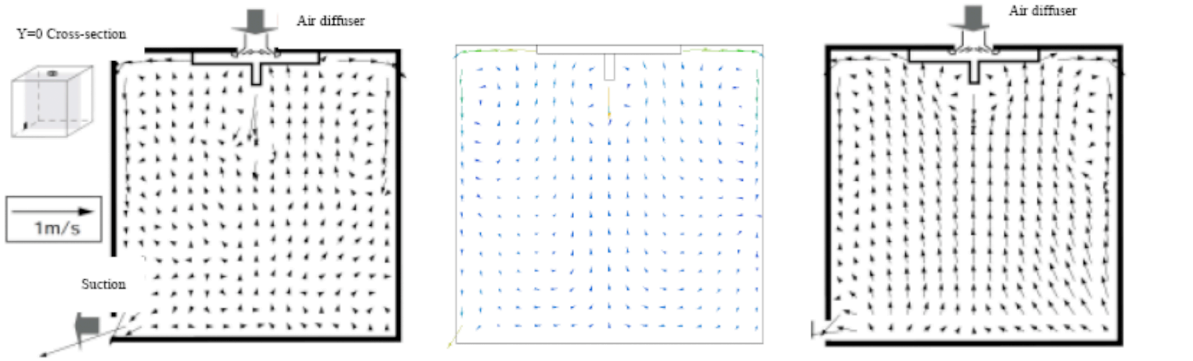

Figure 3: Comparison of experimental and simulation results.

Table 4: Air Diffuser with a Horizontal Blowing Direction When the Number of meshes for Each Side is 16

No.	Normal Component [m/s]	Tangential Component [m/s]	V [m/s]	k [m^2/s^2]	ε [m^2/s^3]	A [m^2]	No. of Locations	Flow rate	
								[m^3/h/1 Location]	Total [m^3/h]
1	1.200	0.076	1.202	0.0517080	0.0152130	0.0025	8	10.8	86.4
2	1.164	0.219	1.184	0.0517080	0.0152130	0.0025	8	10.5	83.8
3	1.098	0.344	1.151	0.0517080	0.0152130	0.0025	8	9.9	79.1
4	1.012	0.443	1.105	0.0517080	0.0152130	0.0025	8	9.1	72.9
5	0.916	0.516	1.051	0.0517080	0.0152130	0.0025	8	8.2	66.0
6	0.819	0.563	0.994	0.0517080	0.0152130	0.0025	8	7.4	59.0
7	0.727	0.591	0.937	0.0517080	0.0152130	0.0025	8	6.5	52.3
8	0.642	0.602	0.880	0.0517080	0.0152130	0.0025	8	5.8	46.2

Table 5: Induced Airflow Boundaries When the Number of meshes for Each Side is 16

No.	Normal Component [m/s]	Tangential Component [m/s]	V [m/s]	k [m^2/s^2]	ε [m^2/s^3]	A [m^2]	No. of Locations	Flow rate	
								[m^3/h/1 Location]	Total [m^3/h]
16	0.203144	0.000	0.203144	0.000412676	1.72189E-06	0.6375	1	466.2	86.4

Table 6: Air Diffuser with a Downward Diffusion Direction When the Number of meshes for Each Side is 16

No.	Normal Component [m/s]	Tangential Component [m/s]	V [m/s]	k [m^2/s^2]	ε [m^2/s^3]	A [m^2]	No. of Locations	Flow rate	
								[m^3/h/1 Location]	Total [m^3/h]
9	-0.200	0.000	0.200	0.0517080	0.0152130	0.0013	4	-0.9	-3.6
10	-0.200	0.000	0.200	0.0517080	0.0152130	0.0013	4	-0.9	-3.6
11	0.000	0.600	0.600	0.0517080	0.0152130	0.0013	4	0.0	0.0
12	0.300	1.100	1.140	0.0517080	0.0152130	0.0013	4	1.4	5.4
13	0.150	1.200	1.209	0.0517080	0.0152130	0.0013	4	0.7	2.7
14	0.200	0.700	0.728	0.0517080	0.0152130	0.0013	4	0.9	3.6
15	1.600	0.300	1.628	0.0517080	0.0152130	0.0013	4	3.6	14.4

Table 7: Air Diffuser with a Horizontal Diffusion Direction When the Number of meshes for Each Side is 8

No.	Normal Component [m/s]	Tangential Component [m/s]	V [m/s]	k [m^2/s^2]	ε [m^2/s^3]	A [m^2]	No. of Locations	Flow rate	
								[m^3/h/1 Location]	Total [m^3/h]
1	1.182	0.148	1.191	0.0517080	0.0152130	0.0050	8	21.3	170.2
2	1.055	0.394	1.126	0.0517080	0.0152130	0.0050	8	19.0	151.9
3	0.868	0.540	1.022	0.0517080	0.0152130	0.0050	8	15.6	124.9
4	0.685	0.597	0.908	0.0517080	0.0152130	0.0050	8	12.3	98.6

Table 8: Induced Airflow Boundaries When the Number of meshes for Each Side is 8

No.	Normal Component [m/s]	Tangential Component [m/s]	V [m/s]	*k* [m^2/s^2]	*ε* [m^2/s^3]	A [m^2]	No. of Locations	Flow rate	
								[m^3/h/1 Location]	Total [m^3/h]
5	0.181	0.000	0.181	0.0517080	0.0152130	0.0400	1	26.1	26.1
6	-0.289	0.000	-0.289	0.000832472	4.9334E-06	0.6000	1	-623.2	-623.2

Table 9: Air Diffuser with a Horizontal Diffusion Direction When the Number of meshes for Each Side is 4

No.	Normal Component [m/s]	Tangential Component [m/s]	V [m/s]	*k* [m^2/s^2]	*ε* [m^2/s^3]	A [m^2]	No. of Locations	Flow rate	
								[m^3/h/1 Location]	Total [m^3/h]
1	1.119	0.271	1.151	0.0517080	0.0152130	0.0100	8	40.3	322.1
2	0.776	0.568	0.962	0.0517080	0.0152130	0.0100	8	27.9	223.5

Table 10: Induced Airflow Boundaries When the Number of meshes for Each Side is 4

No.	Normal Component [m/s]	Tangential Component [m/s]	V [m/s]	*k* [m^2/s^2]	*ε* [m^2/s^3]	A [m^2]	No. of Locations	Flow rate	
								[m^3/h/1 Location]	Total [m^3/h]
3	0.0453	0.000	0.045	2.05322E-05	1.91094E-08	0.1600	1	26.1	26.1
4	-0.361	0.000	-0.361	0.001300738	9.63555E-06	0.4800	1	-623.2	-623.2

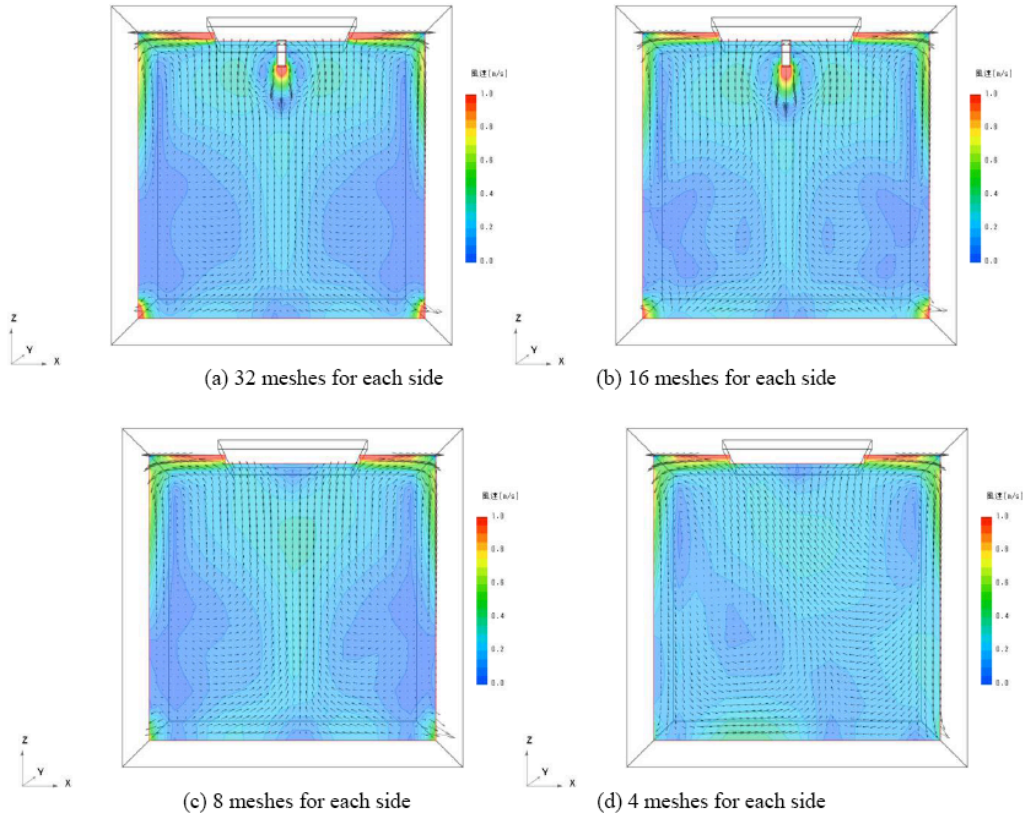

(a) 32 meshes for each side (b) 16 meshes for each side

(c) 8 meshes for each side (d) 4 meshes for each side

Figure 4: Effects of number of meshes on wind speed distributions.

of CFD simulations in the vertical cross-section at Y=0. The CFD analysis results in this study (Figure **3** (**b**)) agree well with the experimental results.

2.2. Simplification of the Boundary Conditions for the Anemostat-Type Air Diffuser

The method in the previous section involved discretizing the virtual boundaries of the air diffuser into 32×32 (1,024 total) mesh, which enabled us to obtain the same results as those in the experiment [4]. However, each air diffuser must be discretized into 1,024 segments, and high-performance computers equipped with multiple CPUs would be needed to perform a CFD analysis on an entire room [5]. In this section, we reduced the number of mesh elements and identified total mesh numbers that could be used to obtain practical and usable solutions. We considered four mesh designs: 32, 16, 8, and 4 elements for each side. Tables **4–6**, **7–8**, and **9–10** show the air diffuser conditions for the mesh with 16, 8, and 4 elements for each side, respectively. Since the mesh intervals were large in the cases of 8 and 4 segments, we simplified the lower rod that supplied air downward from the center of the air diffuser; see Figure **1**.

Figure **4** shows the airflow velocity vectors for each case where the cross section is the same as in Figure **3**. If we exclude the downward airflow below the diffuser, the general flow pattern in the space is symmetrically distributed; however, some of the symmetry started to fade in cases where only 4 mesh partitions were used for each side. Figure **5** shows the wind velocity (velocity magnitude) at heights of FL+1,200, FL+800, FL+400 (FL represents zero of z axis) for each of the same cross-sectional positions. The same trends are observed for heights of FL+800 and less, only the case where there were 4 mesh

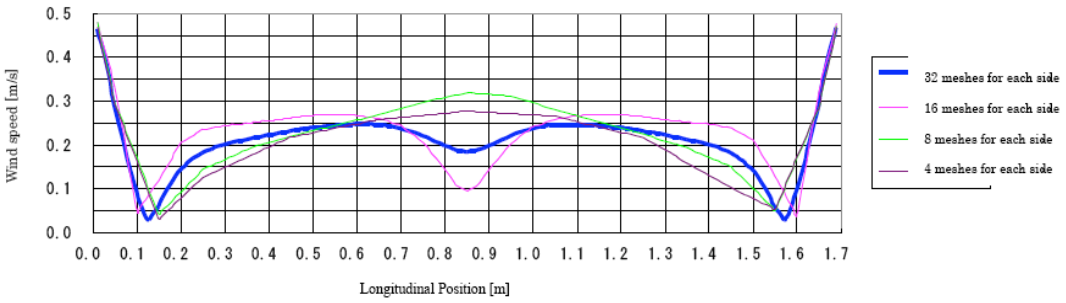

(a) FL+1,200

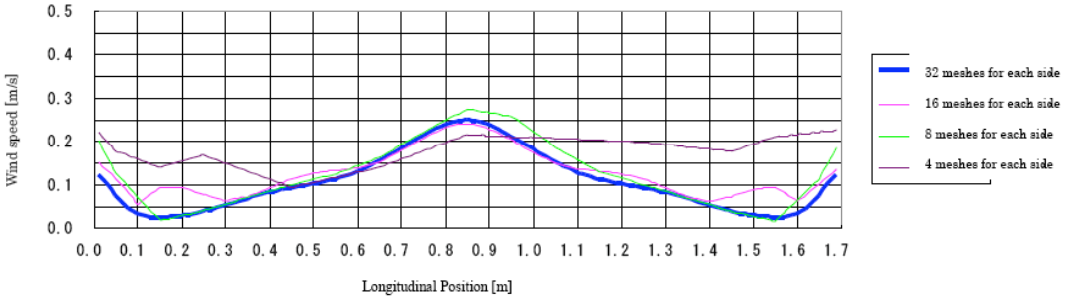

(b) FL+800

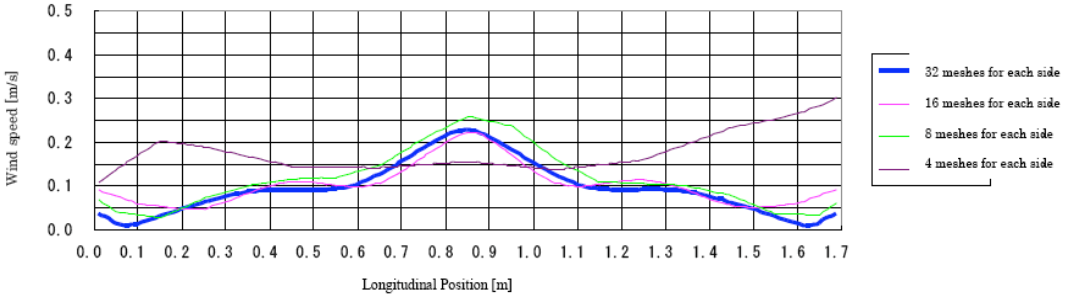

(c) FL+400

Figure 5: Effects of number of partitions on wind speeds at each height.

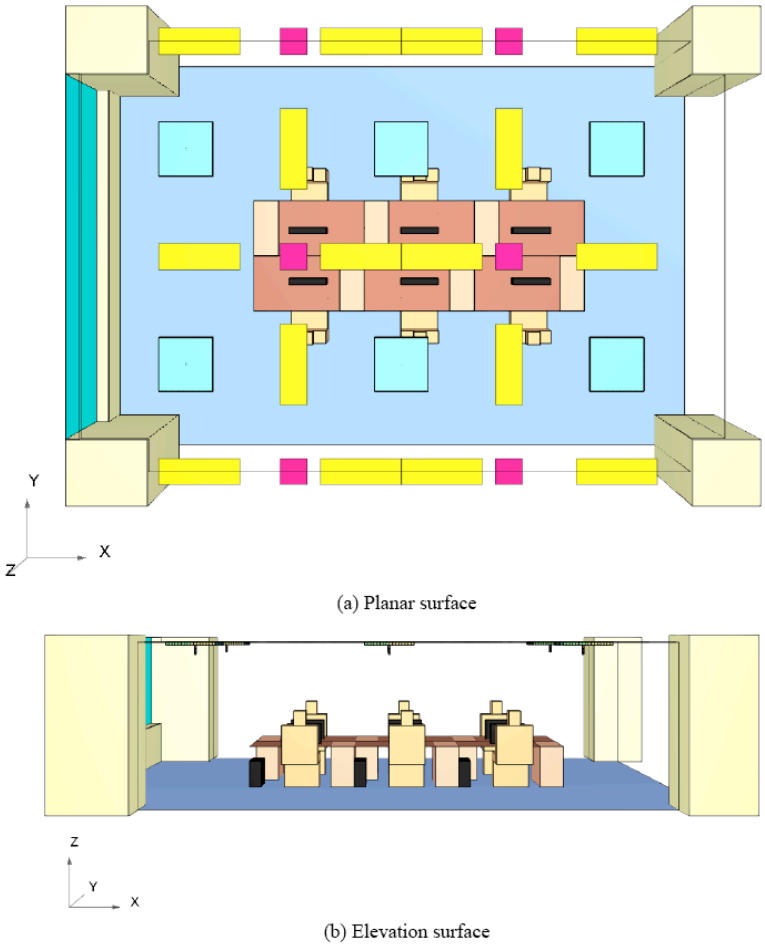

Figure 6: Computational model of an office room for analysis.

partitions for each side greatly differed from that using 32 mesh discretization. The results indicate that to reproduce the general flow the number of mesh elements could be reduced to 8 for each side, and, to reproduce the airflow right below the air diffuser, the number could be reduced to 16 for each side.

2.3. Application to Office Spaces

We carried out a study on the number of mesh elements for the air diffuser and evaluated applications to air-conditioned spaces that were assumed to be one span of a room subjected to peripheral loads and internal heat loads.

Figure **6** shows the computational domain representing an office room. The dimensions are: *x*-direction: 9.6 m, *y*-direction: 6.4 m, and *z*-direction: 2.6 m. Air diffusers were placed at six locations (blue-green squares in the middle of Figure **6**(**a**)), air inlets at four locations (pink squares), lighting at 16 locations (yellow rectangles; however, the area was half on the wall-surface boundary), and human bodies and office automation (OA) devices at six locations each. Additionally, window panes were positioned on the left side in Figure **6**(**a**). Table **11** details the thermal load conditions, and Table **12** the air-conditioning conditions. The commercial CFD code (CRADLE/STREAM) and turbulence model used here are the same as those in previous section 2.2. Table **13** summarizes the total number of mesh elements for each case. The total mesh elements for the case where the air diffuser with four partitions for each side was 1/100 of that when it was set to 32 partitions for each side.

Figures **7-10** shows temperature distributions and velocity magnitudes for the longitudinal cross section that passes through the center of the air diffuser. The velocity magnitudes in Panels (a) of each Figure had overall velocities of 0.2 m/s or less; wind speeds were slowest in regions around the human heads. The velocity magnitudes also show slight increases for flows that continued to move downward. There were no significant differences between the cases for the rest of the fluid region. The temperature distributions found in

Table 11: Thermal Load Conditions

(a) Structural Load
<Lower wall (Wall Type:
· Place: Tokyo, Azimuth: S, Season: Summer, Time: 2:00pm, Coefficient for heat transfer: 1.0W/m2·K, Effective Temp.: 40°C
· Area: (5.4 m(W) °— 0.8 m(H)) + (5.4 m(W) °— 0.2 m(D)) = 5.4 m2
<Glass (Low-E)>
· Outside Air Temp.: 33.4°C, Coefficient of Heat Transfer: 2.6 W/m2·K
· Area: 5.4 m(W) °— 1.8m(H) = 9.72 m2
<Outer Pillar>
· Temperature of non-air-conditioned spaces (Inside of column) : (40°C − 26°C)/2 + 26°C = 33°C
· Area: (2.86 m2 + 1.25 m2) °— 2 columns = 8.22 m2
· Column Wall Thickness: 10 mm, Column wall material: Mortar (Heat Conductivity: 1.5 W/m·K)
→Heat Transfer Coefficient: 1/(1/9.3+0.01/1.5+1/9.3) = 4.5 W/m2·K
(b) Insolation (Solar Radiation) Load
· Glass type: Low-E, Reflectance Ratio: 18.9%, Transmissivity: 52.1%, Absorptance: 29.0%, Shading Coefficient: 0.48
· Area: 5.4 m(W) °— 1.8 m(H) = 9.72 m2
· Location: Tokyo, Azimuth: S, Solar altitude: 57.03°, Season: Summer, Time: 2:00 pm
→Amount of solar radiation in the entire sky: 205 W/m2
· Heat Conductivity of Glass Outer Surface: 23.3 W/m2·K, Inner Surface: 9.3 W/m2·K
→The proportion of glass absorption components which penetrated the indoor area: (1/23.3)/(1/23.3+1/9.3) = 0.285
(c) Human Body Load
· Amount of Heat assumed to be generated while working: 55 W/person (Dissipated heat)
· Number of People: 6
(d) Lighting Load
· 30 W × 2 pieces = 60 W/piece
· Number of devices: 8 pieces + 8 pieces × 1/2
(e) OA Instrument load
· Computer Unit: 60 W/unit, Computer Monitor Unit: 50 W/unit
· Number of units: 6

Table 12: Air-Conditioning Conditions

(a)SA
· Air Volume: 2,797.2m^3/h (Circular Anemostat: 6 units, 466.2m^3/h·unit)
· Air diffuser Temperature: 23.58 °C
(b)RA
· Air Volume: 2,797.2 m^3/h (VHS 400 × 400 × 4 units (Inside of analyzed area), 744.8m^3/h/unit))

Table 13: Total Mesh Number for Each Case

Case	Total Number of Meshes			
	x	y	z	Total
32 meshes for each side	286	188	81	4,355,208
16 meshes for each side	206	133	54	1,479,492
8 meshes for each side	98	66	31	200,508
4 meshes for each side	50	36	21	37,800

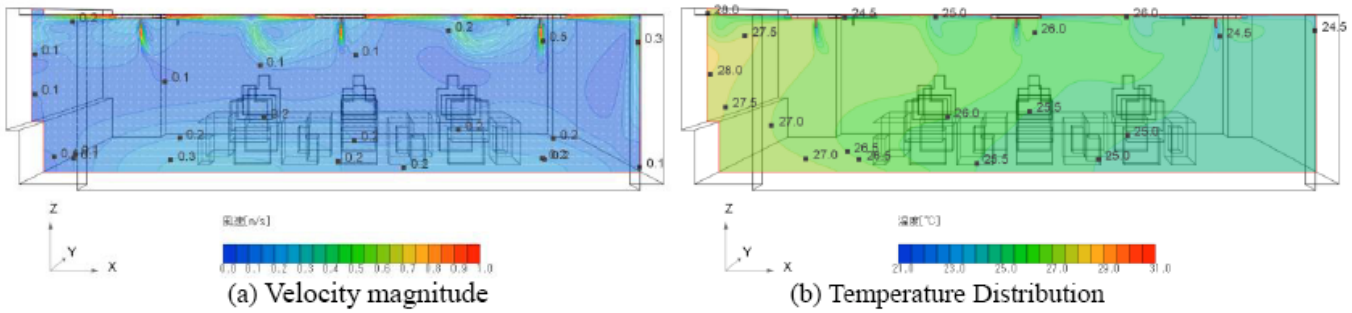

Figure 7: Distribution of the longitudinal cross section for the center of the room where the air diffuser was discretized into 32 meshes for each side.

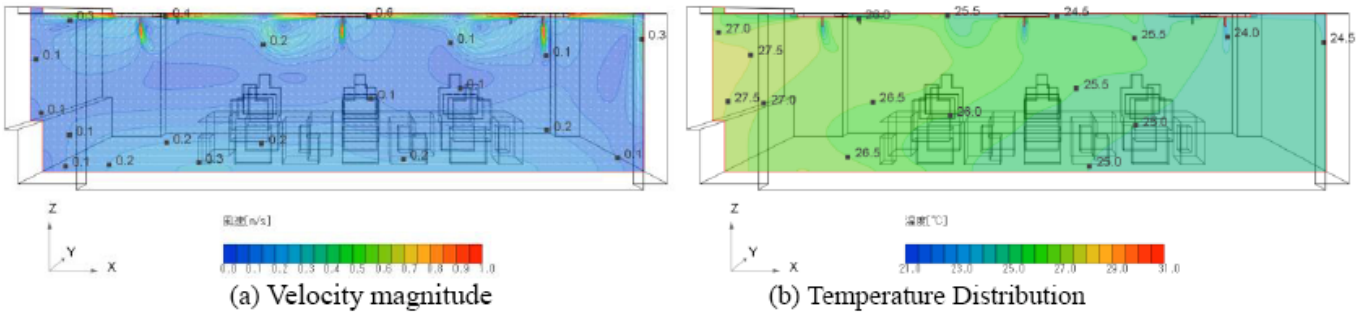

Figure 8: Distribution of the longitudinal cross section for the center of the room where the air diffuser was discretized into 16 meshes for each side.

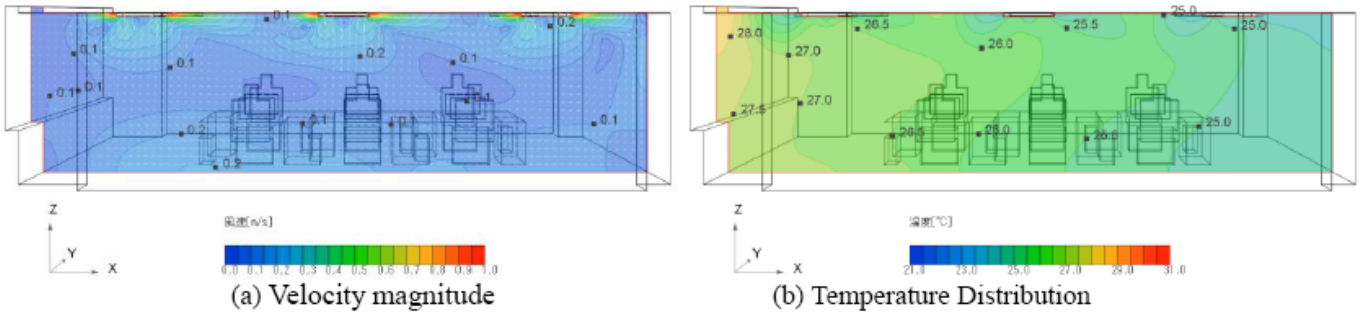

Figure 9: Distribution of the longitudinal cross section for the center of the room where the air diffuser was discretized into 8 meshes for each side.

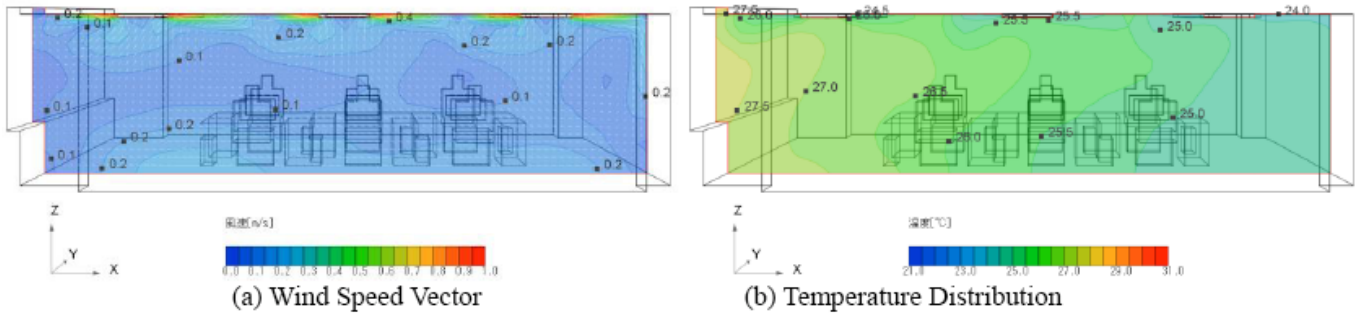

Figure 10: Distribution of the longitudinal cross section for the center of the room where the air diffuser was discretized into 4 meshes for each side.

Panels (b) of each Figure all showed thermal gradients forming along the areas from the perimeter toward the interior. The temperature was 27°C around the perimeter and 25°C at the interior. There were no significant differences seen among the cases for temperature distributions.

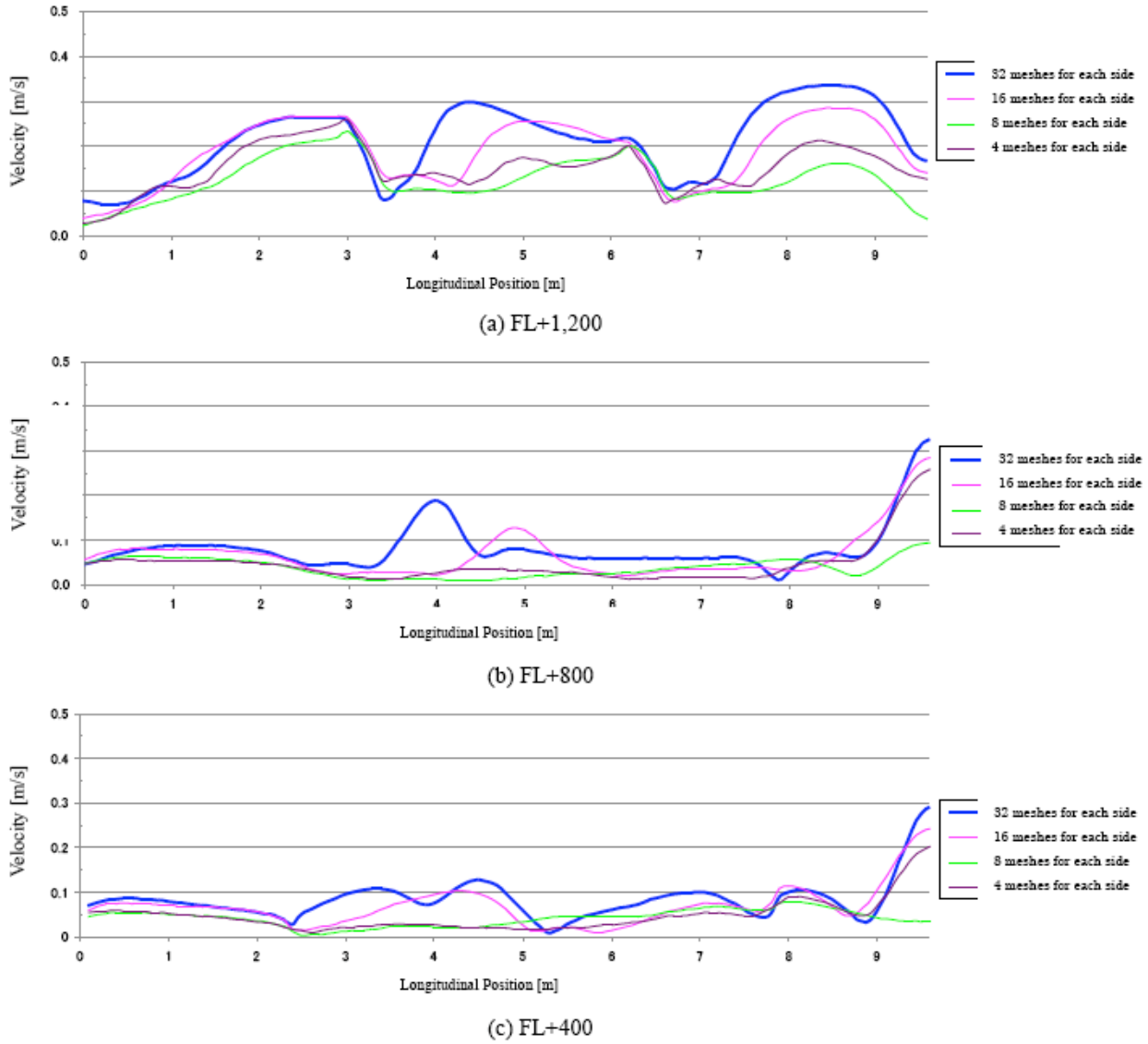

Figure 11: Scalar velocities for each height.

Figures **11** and**12** show temperatures and velocities (velocity magnitude) at FL+1,200, FL+800, FL+400 for each of the cases at the same cross-sectional location. The regions with high velocities increased its velocity further as the number of mesh increased, while the velocities became more uniform as the number of mesh partitions decreased. However, the velocities remained 0.25 m/s or less in almost all areas, and we confirmed that the first-order airflow coming from the diffuser did not affect the velocity. For the temperature profile, a 3°C decrease in the area from the window surface toward the interior area was found. In general the temperature profiles were similar except for one position at longitudinal position of 4m.

Since it possible to reproduce the overall trends, even if the number of mesh partitions for the air diffuser is reduced to four on each side, we can say that prediction accuracy is high enough for use in practical applications. Additionally, when the number of mesh partitions for the air diffuser was set to 4 for each side, the plane area of the analyzed space was about 62 m^2, and the total number of mesh was about 38,000. Using the method described in this study, it would be possible to perform a CFD analysis of an entire 2,000-m^2 glass office using a 32-bit personal computer.

2.4. Discussions

We concluded that the most difficult parts of developing boundary conditions for a circular Anemostat-type air diffuser include the following: (1) methods for implementing virtual air diffusers, and (2) establishing ranges over which visualization are possible. Since it is possible to reduce the total number of meshes through simplification, it is also possible to

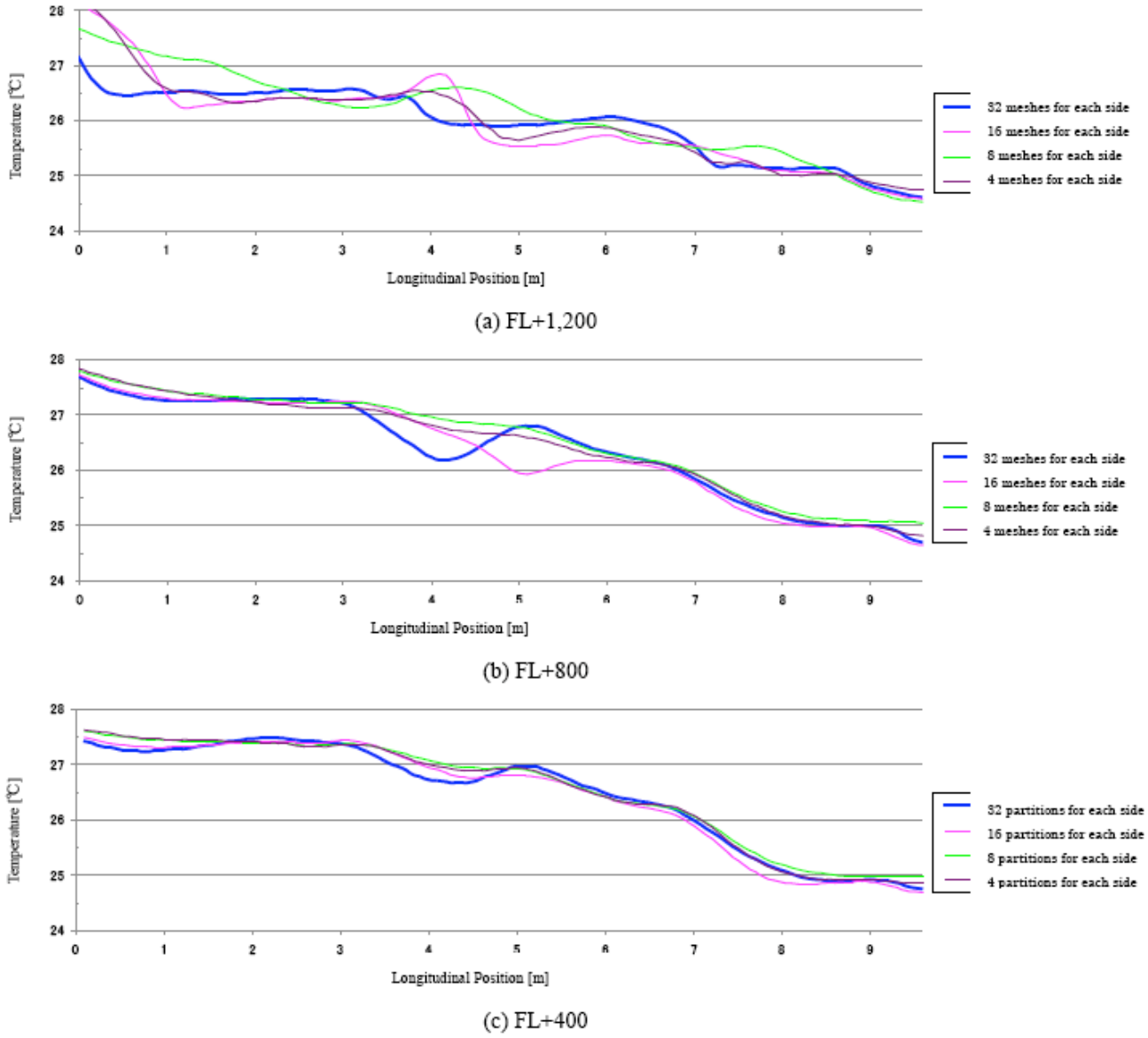

Figure 12: Temperatures for each height.

perform an analysis of a larger space using a computer with the same performance characteristics. The outcomes in this section are summarized as follows:

- To precisely reproduce the supplied airflow, the air diffuser model must be discretized into at least 16 segments (meshes) on each side.
- To estimate a general supplied airflow from the diffuser, the virtual air diffuser must be discretized into at least 8 segments on each side.
- To estimate airflow and temperature distributions in an air-conditioned space, it is possible to reduce the number of meshes for each side of the virtual air diffuser to at least 4 segments. In such cases, a 32-bit personal computer can be used to perform a CFD analysis of an entire 2,000-m^2 glass office building.

3. KITCHEN AIRFLOWS

In recent years, changes in lifestyle have led to improvements in residential kitchens. For example, modern residential kitchens may be equipped with induction heating (IH) devices or high-efficiency gas devices. There is also greater variety in cooking devices used in commercial kitchens compared with that found in the average residential kitchen. To study the thermal and airflow environments found in these kitchens, we need to accurately reproduce the hood-trapping characteristics for thermal plumes (upward airflow) that originate during cooking.

In previous research using CFD analysis for kitchens, the total heat flux have been defined as boundary conditions on areas of the heat sources such as cooking devices. However, previous studies [6] suggested that this approach often underestimates the thermal plume width and may overestimate hood-trapping properties.

As a result, Kondo *et al*. [7] recommended a modeling method involving measuring wind velocity distributions of thermal plumes near the top of a variety of pots placed on gas cookers in residential kitchens and defining the measured values using CFD analysis. In addition, Momose *et al*. [8] proposed another method involving the measuring wind velocity distributions of thermal plumes near the top of a variety of pots placed on gas and IH cookers and defining the statistic values for the velocity and turbulence as boundary conditions for CFD.

In this section, we report and discuss the results from the thermal plume modeling by Kondo *et al*. [6,7] in a kitchen environment. The results are compared between the cases with and without the thermal modeling technique. In addition, we determined whether radiation has any effect on the environment.

3.1. Outline of the Analysis

The dimensions of the kitchen were width = 6.5 m, length = 6.5 m, and height = 2.5 m, shown in Figure **13**. Cooking devices were placed in the middle of the room, and the overhang of the canopy hood was positioned directly above the cooking devices (0.6 m × 0.45 m).

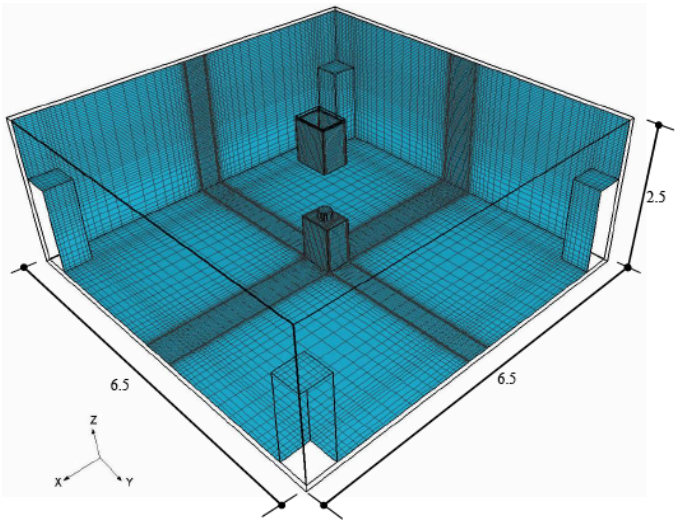

Figure 13: Kitchen model (unit: m).

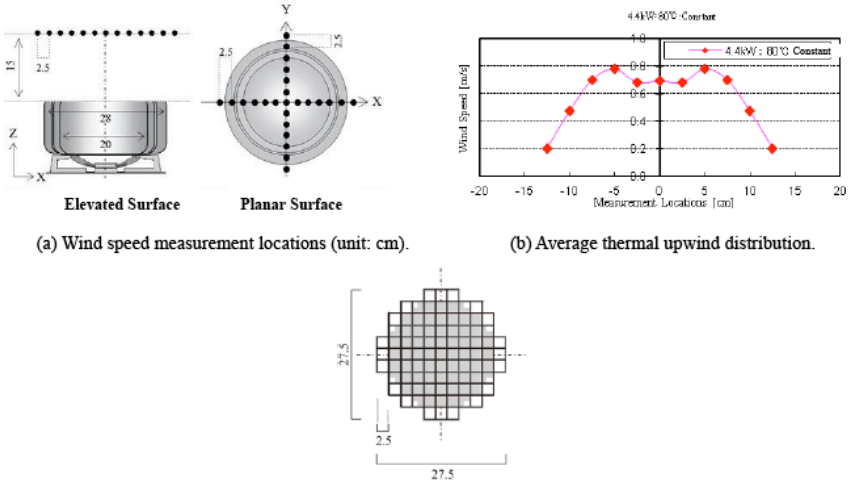

(a) Wind speed measurement locations (unit: cm). (b) Average thermal upwind distribution.

(c) Wind speed-regulated surface at 15 cm above the pot (unit: cm)

Figure 14: Thermal upwind model for the pot. (Example where the following settings were made: 23 cm SUS Pot, heat generation 4.4 kW).

Table 14: Numerical and Boundary Conditions

Analyzed Area		6.5m×6.5m×2.5m (h)
Mesh		87 (x) ×93 (y) ×61 (z) =493,551 Mesh
Computational Cod		Code C
Turbulence Model		Standard k-ε model
Difference Scheme		QUICK
Wall Surface Conditions	Speed	Generalized log law
	Temp	[Convection/Radiation-Coupled Analyses] α_c (convection heat transfer coefficient) was 100 W/ (m^2·k) for the pot surface (The value adjusted to make the pot surface temperature reach 200°C), other wall surfaces: 4.6 W/ (m^2·k) ε (Emissivity): 0.9 for the total wall surface
Inflow Conditions		[Airflow from the 4 (total of 8 Surfaces) supply openings] U_{in}=0.02025m/s (Q_{in}=36.45m^3/h/Surface) , T_{in}=25.0℃, K_{in}=9.0E-04m^2/s^2, ε_{in}=8.873E-06m^2/s^3 Air supply surface: 0.5m×1.5m
Outflow Conditions		[Hood Exhaust] U_{out}=0.3m/s (Q_{out}=291.6m^3/h) , Hood Hs: 0.6 m×0.45 m×0.7 mh (Overhang: 0 m) Exhaust surface: 0.6 m×0.45 m, interval distance for the cooking units: 1.0 m
Heat Generation Conditions		[Heat Generation of a Pot] Calorific value: 2.7 kW (The value after subtracting the latent heat when using 4.4 kW.) Volume heat generation for a 23-cm pot model (0.25 m × 0.25 m × 0.15 mh) [Heat Upward Flow] Regulation of thermal upwind wind speed (y) 15 cm above the pot by using the following approximation formula: $y=0.7-8.62x+461.04x^2-6362.1x^3+23826x^4$ Here, x: horizontal distance from the center of the pot (m)

Table 15: Cases Analyzed

Case Name	Thermal Modeling	Radiation Analysis
Case A	No	No
Case A-M	Yes	No
Case A-M-R	Yes	Yes

The hood displacement (exhaust capacity of the hood) was set to 291.6 m^3/h, which corresponds to an average surface wind speed of 0.3 m/s. Air was supplied from the four corners of the room at a total flow rate of 72.9 m^3/h. The calorific value (total heat generation rate) for the pot was 2.7 kW and the thermal plume model proposed by Kondo *et al*. [6,7] was used. Figure **14** shows the vertical distribution of upward airflow speeds for thermal plume at 15 cm above the top of the pot used for the boundary condition and Table **14** summarizes the CFD settings. In this analysis, the commercial CFD software, CRADLE/STREAM – Code C was used.

3.2. Cases Analyzed

Three scenarios were performed: Case A did not involve any thermal plume modeling, Case A-M included thermal plume modeling, and Case A-M-R included both thermal plume modeling and radiation heat transfer. These are summarized in Table **15**.

3.3. Analysis Results

Figure **15** shows temperature distributions for the two cases, where the width of the thermal plume is marginally smaller when thermal modeling is neglected (Case A). Additionally with thermal modeling (Case A-M) higher temperatures are found in areas near the ceiling, due to the increased plume overflowing from the hood.

Figure **16** shows concentration distributions of a passive scalar generated from the pot surface. The ventilation intake generated a distribution for the passive scalar. The inclusion of thermal plume modeling caused by the heat source (e.g. pot surface) had significant impact on temperature and scalar concentration distribution around the exhaust hood

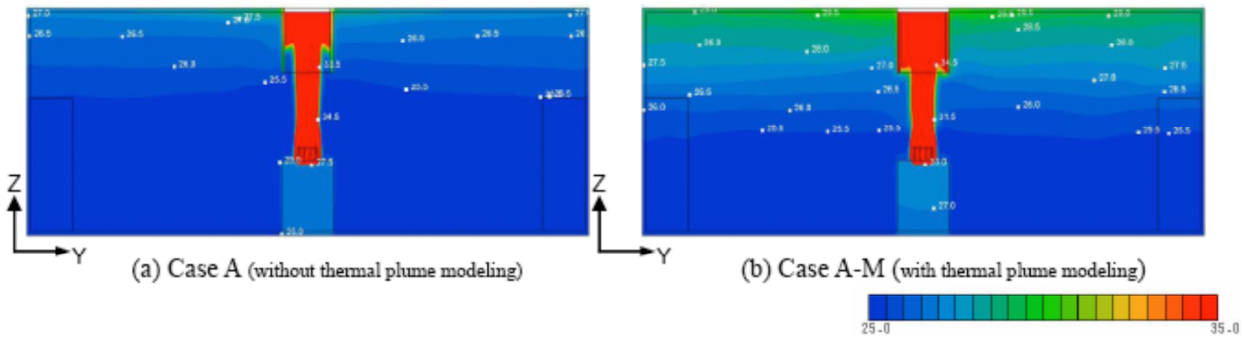

Figure 15: Temperature distributions (X = 3.25) unit: [°C].

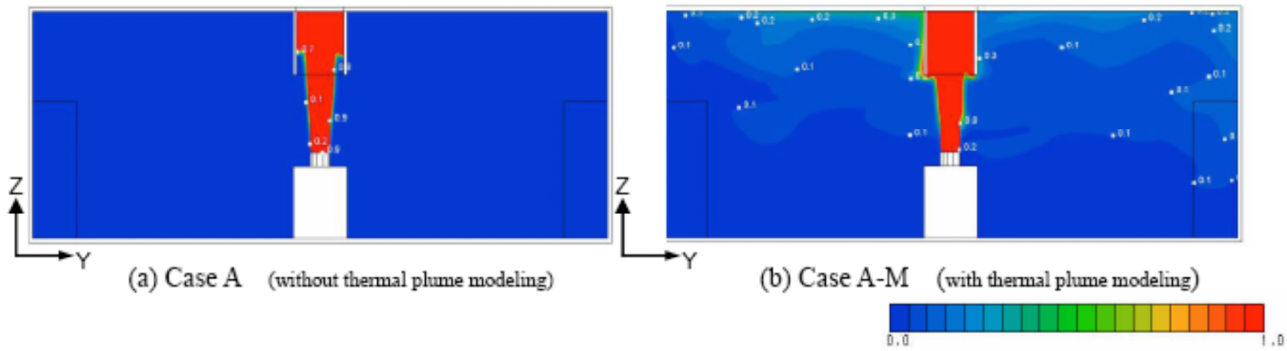

Figure 16: Dimensionless concentration distributions (X = 3.25) unit: [-].

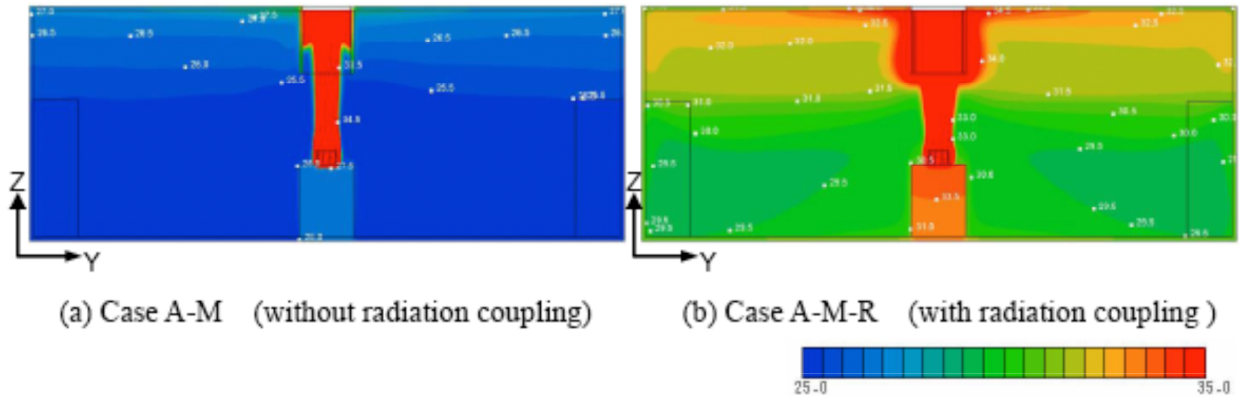

Figure 17: Temperature distributions (X = 3.25) unit: [°C].

canopy. The predicted results in the trapping efficiency of the canopy hood seem to be greatly influenced by the thermal plume.

The effects of radiation were studied by comparing Case A-M-R (with radiation) and Case A-M (without radiation). Figure **17** shows that spatial temperatures for Case A-M-R were about 4–6°C higher overall than for Case A-M. This may have been caused by the wall surfaces heated through radiant heat transfer.

Figure **18** shows, for all three cases, vertical temperature distributions in a region 1.5 m from the center of the pot.

The vertical temperature distributions in suggest that, in Case A, the hood trapped most of the thermal plume, resulting in a small vertical temperature distribution. In contrast, thermal plumes in Cases A-M and A-M-R overflowed from the hood, causing vertical temperature distributions to grow larger.

3.4. Discussions

We evaluated how radiation and models of thermal plume (upwind flow) affect results from CFD simulations of a residential kitchen, with the following findings:

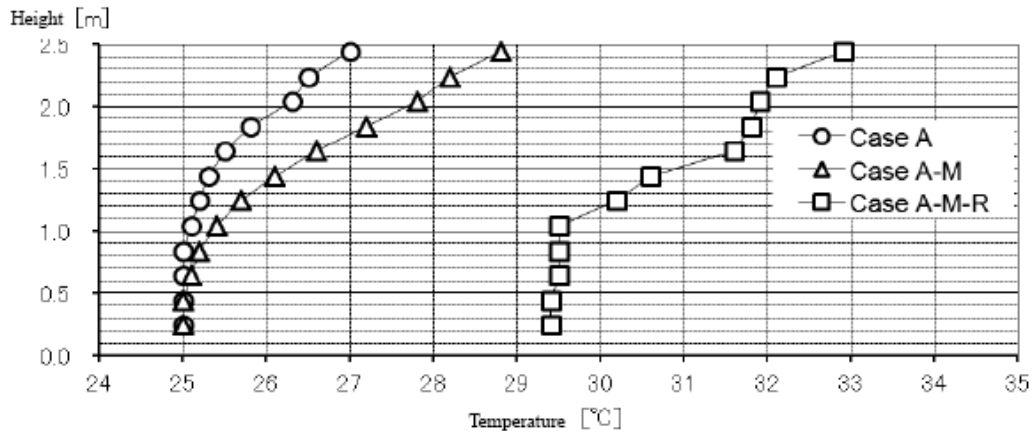

Figure 18: Vertical temperature distributions at the point 1.5 m (Y = 4.75) apart from the center of the pot.

- Without thermal plume modeling, hood-trapping capacity was overestimated. This may be due to underestimation of exhaust capacity of the hood.

- Without radiation analysis, spatial temperatures decreased. This may be due to underestimation of the air-conditioning load.

Previous studies have, to some extent, improved experimental data on thermal plumes generated from cooking devices in kitchens. However, validation data for airflows and temperature distributions around the hood and inside kitchens are not available. Therefore, we were not able to obtain CFD results that are consistent with experimental data. After obtaining validation data for kitchen environments, we plan to compare those data with CFD results.

4. FIRE-INDUCED AIRFLOW

4.1. Objectives and Problems

Fires are extremely complicated unsteady phenomena accompanied by convection induced by combustion. Combustion can cause large changes in air temperatures and emit radiant heat. Consequently, fire modeling has disadvantages such as a wide variety of conditions that must be considered and the boundary conditions are often difficult to determine. For this reason, almost no optimal experimental results are suitable for validation and verification of the results of CFD analyses. Against this background, for easy comparison with the results of CFD analyses, Kato *et al*. [9] and Murakami *et al*. [10] performed a series of experiments with high-temperature natural convection by setting well-defined clear boundary conditions

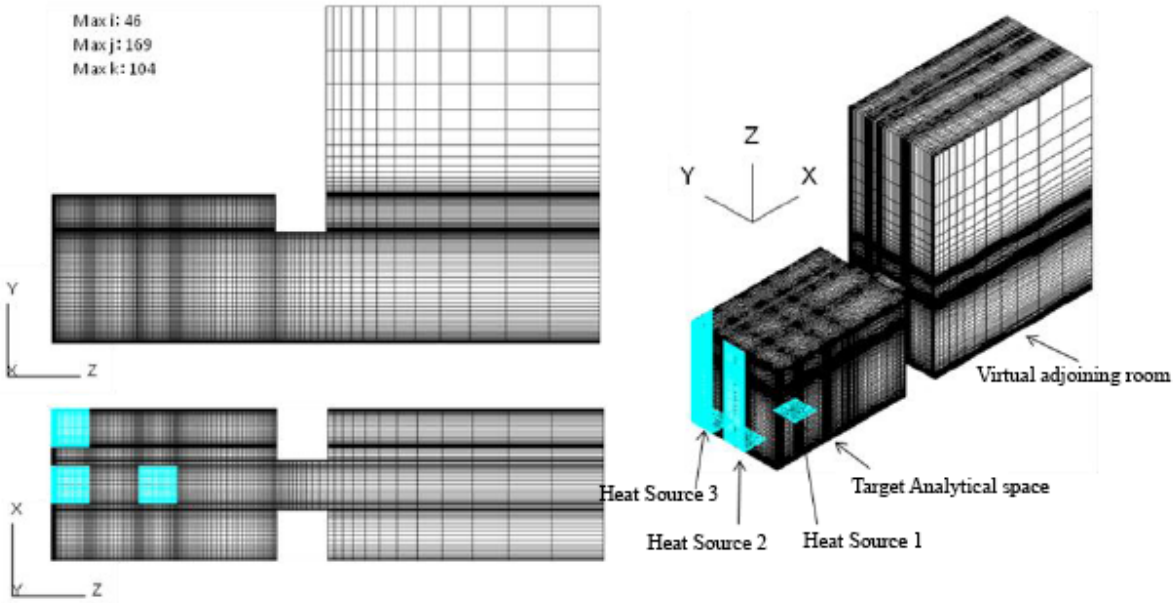

Figure 19: Analytic model.

without using actual fire. This section describes the results of benchmark tests, performed using CFD to compare with the experiments results.

4.2. Subject of Analysis and Condition Settings

The computational domain was a single-room model of a burning room (Figure **19**). The model includes a virtual adjoining room connected to a burning room to simulate the phenomenon, which may occur on the outside of the room in case of fire. The number of grid partitions for the model was set to 46(i) × 169(j) × 104(k). In the experiments, three heating planes (sources), which served as combusting surfaces were placed in the room [9,10]. The boundary conditions of the heating planes (sources) were set as:

- Heat source 1: at the center of the floor surface (calorific value 1.1 kW),
- Heat source 2: wall surfaces and floor surfaces in the vicinity of them (calorific value 5.4 kW),
- Heat source 3: wall surfaces and floor surfaces in corners (calorific value 9.1 kW).

Fourteen measurement points for wind velocity and temperature along seven vertical lines were used (Figure **20**). These measurement points were set such that they correspond to those used in the experiments by Murakami *et al*. [10].

Seventeen simulation cases were conducted, summarized in Table **16**. Two CFD codes, CRADLE/STREAM (Code C) and STAR-CD (Case D) were used. To simulate fire-induced airflow with large differences in temperature depending on the measurement points, the airflow should be assumed to be a compressible fluid. However, for indoor airflow simulations, an incompressible viscous fluid and buoyancy effects may be represented by the Boussinesq approximation; therefore, these simulations were conducted using the fundamental equations for both compressible and incompressible fluids.

Simulations were conducted using three heat sources (sources 1 to 3) described in Figure **20**. Methods that use a heat flux for exothermal boundaries have been widely studied. In addition, we have obtained detailed measurements for temperatures on the exothermal surface, so we also conducted

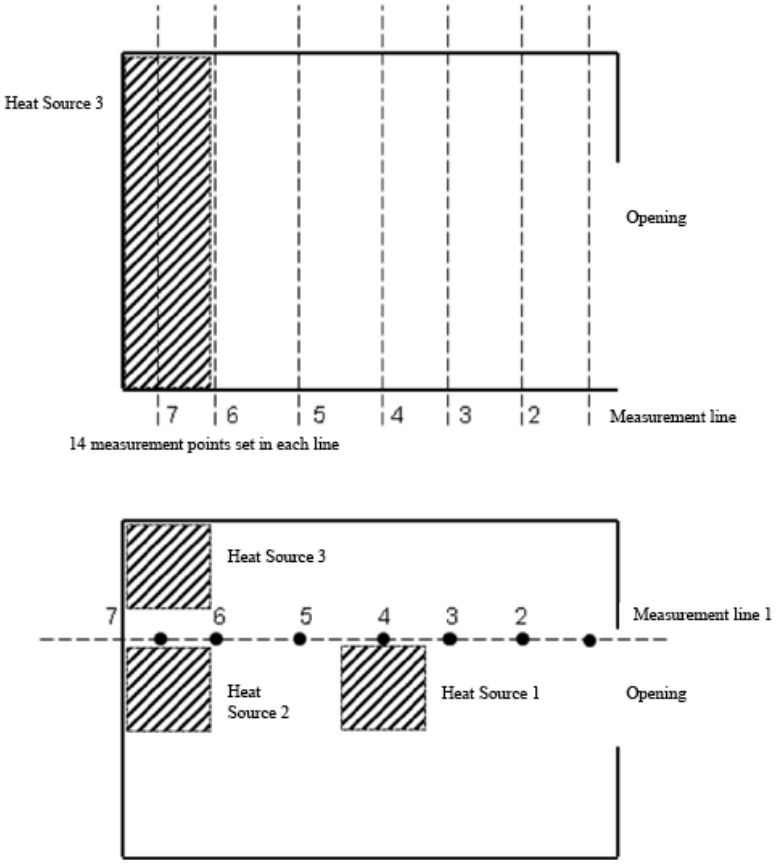

Figure 20: Measurement points and horizontal line connecting them.

Table 16: Simulation Codes, Models, Boundary Conditions, etc. That were Used in each of the 17 Simulations Performed in This Study

	Analysis Code	Fundamental Equation	Exothermal Location	Exothermal Conditions	Hypothetical Adjacent Room Boundaries	Used Radiation Analysis Coupling?	Turbulence Model
CASE-1	Code D	Uncompressible	Heat source No. 1	Heat flux	Boundary Condition No. 2	Yes	Standard k–ε
CASE-2			Heat Source No. 2		Boundary Condition No. 1		Low-Re k–ε model
CASE-3							RNG k–ε
CASE-4					Boundary Condition No. 2		Standard k–ε
CASE-5							Low-Re k–ε model
CASE-6							RNG k–ε
CASE-7						No	Standard k–ε
CASE-8							RNG k–ε
CASE-9		Compressible				Yes	Standard k–ε
CASE-10		Uncompressible		Fixed Temp.			Low-Re k–ε model
CASE-11			HS No. 3	Heat flux			Standard k–ε
CASE-12	Code C		HS No. 1				
CASE-13			Heat source No. 2				Low-Re k- ε model
CASE-14							RNG k–ε
CASE-15							Standard k- ε
CASE-16			HS No. 3				
CASE-17							

simulations using those measured values as fixed-temperature boundary conditions.

Since both inflows and outflows coexist at the boundaries of hypothetical adjacent rooms, the boundaries can be difficult to calculate. We tested two configurations for boundary conditions: (1) in Boundary Condition 1, we considered all hypothetical boundary surfaces (with the exception of floors) to be free inflowing and outflowing. (2) In Boundary Condition 2, we set limitations on the scope of these inflow and outflow boundaries. We used sliding walls as hypothetical surfaces (with the exception of the free inflow/outflow boundaries) in Boundary Condition 2.

As temperature variations increase considerably in fires, it is important to take radiation into consideration when performing the analyses. Results with and without radiation were included and compared with the experimental data. We also compared and contrasted results from the following three turbulence models: standard k–ε, low-Re k–ε model (linear), and RNG k–ε.

4.3. Simulation Results

The simulation results from each case in Table **16** provide vertical cross sections, and air velocity, and temperature distributions along sampling points shown in Figure **20**.

4.3.1. Differences Due to Different Boundary Conditions for the Hypothetical Surrounding Rooms

Figure **21** shows simulation results using Boundary Condition 1, and Figure **22** for Boundary Conditions 2 comparing the three turbulence models (standard k–ε model, low-Re k–ε model, RNG k–ε model). There were significant effects on the results due to the boundary conditions for the hypothetical surrounding rooms. These effects were particularly significant for high-temperature in the hypothetical surrounding room; which were caused by flow from the burning room. In addition, although there were differences in the influx (inflow) of low-temperature air flowing into areas near the floor of the burning room, on implementing Boundary Condition 2, low-temperature air started flowing toward the back of the burning room.

Figure **23** compares vertical distributions of temperature and *x*-direction average air velocity from the standard k–ε model using Boundary Condition 1 (Case 2) and Boundary Condition 2 (Case 5). Although the simulations captured the general trend from the experiment many differences are found. The boundary conditions seem to have comparatively small effects on the burning room; however, due to differences in the influx airflow, we see clear differences in the airflow velocity near the floor along measurement line A1.

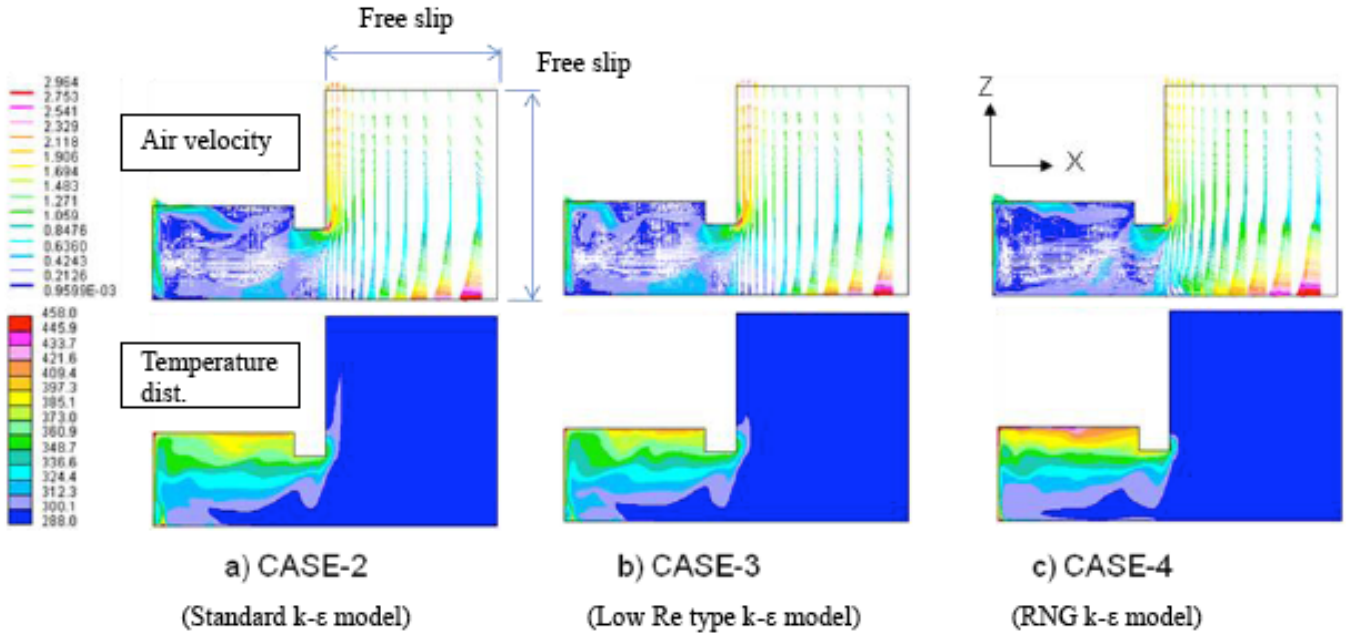

Figure 21: Two-dimensional air speed distributions from the burning room into an adjacent room from simulations using boundary condition 1. (a) Case 2: Code D, standard k–ε model. (b) Case 3: Code D, low-Re k–ε model. (c) Case 4: Code D, RNG k–ε model.

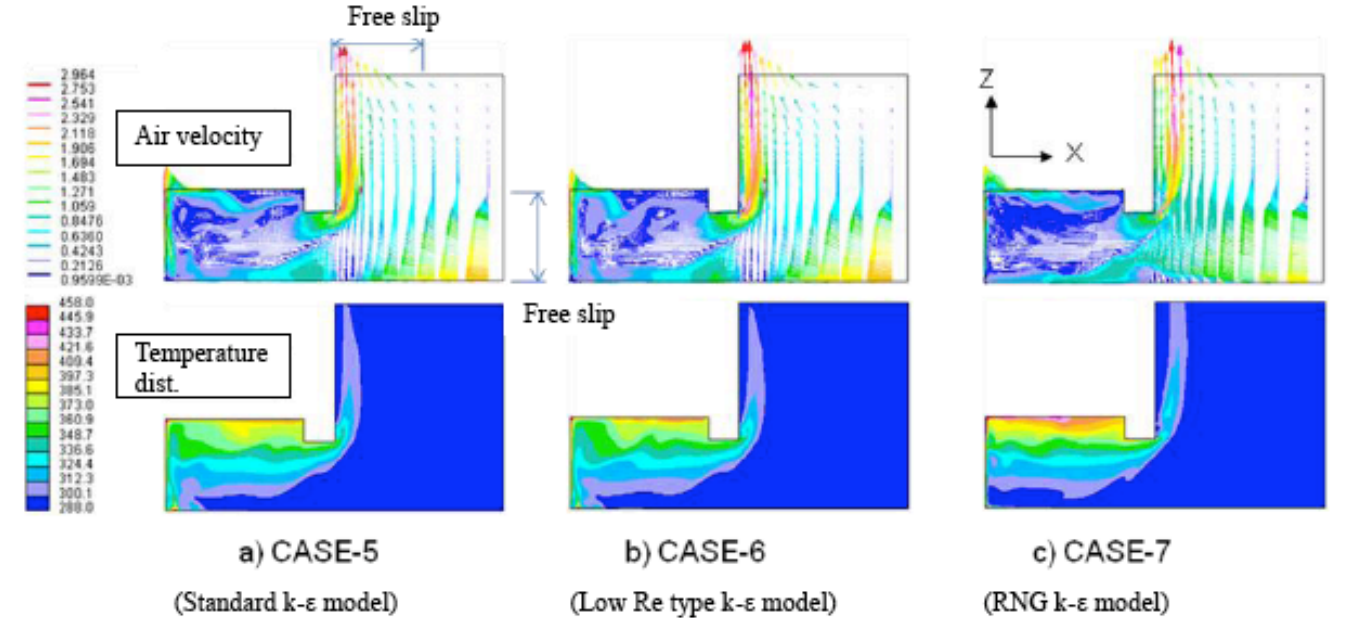

Figure 22: Two-dimensional air speed distributions from the burning room into an adjacent room from simulations using boundary condition 2. (a) Case 5: Code D, standard k–ε model. (b) Case 6: Code D, low-Re k–ε model. (c) Case 7: Code D, RNG k–ε model.

When Boundary Condition 1 was used, the simulation underestimated the velocity near the floor at the back of the burning room. In addition, it was extremely difficult to maintain convergence stability when Boundary Condition 1 was applied. However, with Boundary Condition 2 we managed to complete fairly stable calculations.

4.3.2. Differences Due to Different Computational Codes

Code D was mainly used in these studies; however, comparisons were made with Code C under the same setup using Boundary Condition 2. Results from Code C are shown in Figures **24** and **25**. Although we evaluated all three turbulence models in combination with Code C only two of the turbulence models produced viable results (the low-Re k–ε model did not).

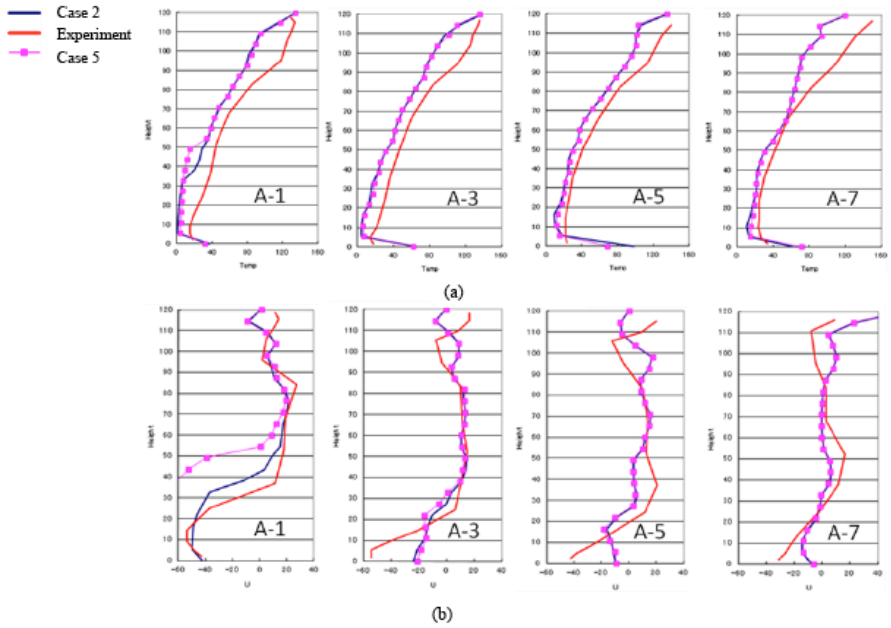

Figure 23: Profiles of (a) temperature and (b) velocity from experiment (red lines), simulations using boundary condition 1 (blue lines), and simulations using boundary condition 2 (lines with points). Case 2: standard k–ε with boundary condition 1. Case 5: standard k–ε with boundary condition 2.

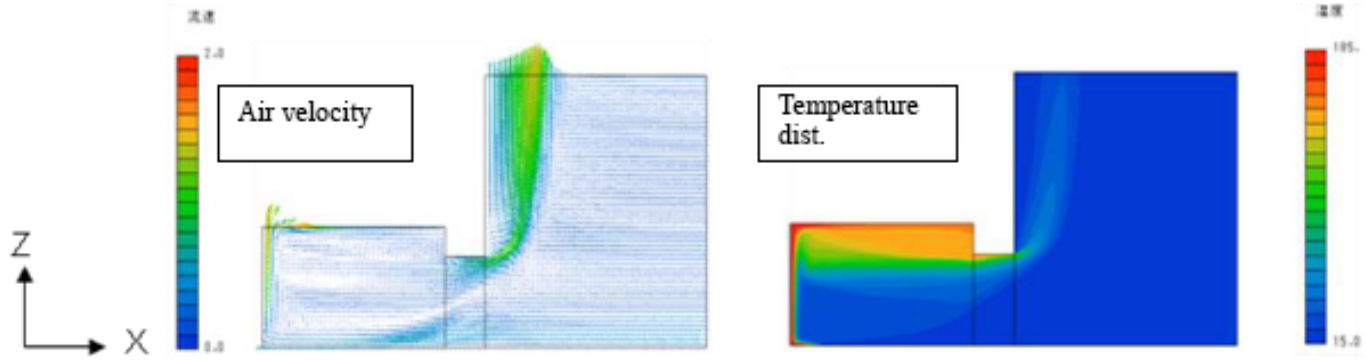

Figure 24: Two-dimensional air speed distributions from the burning room into an adjacent room from simulations using computational Code C. Case 14: Code C, standard k–ε model.

Results earlier from Code D showed large variation in temperature and velocity distributions inside the burning room, but code C produced more smooth distributions for both the temperature and velocity. There were also large qualitative differences in the simulation results. Code C showed an influx of low-temperature air coming into and reaching the back of the burning room. The range of this low-temperature region was significantly larger in results from Code C than from Code D.

Temperature and velocity profiles from Code C are shown in Figure **25** (Code D results also included) which shows an over-prediction of temperature in the upper area of the room and under-prediction in the lower area. In addition, we were only able to reproduce a rapid decrease in the velocity near the floor by using the RNG k–ε turbulence model together with Code D (Case 7).

4.3.3. Differences Based on Location of the Heat Source

In all the simulations described thus far (Figures **21–25**), only heat source 2 was used (see Figure **20**). We now consider how computational results were affected by changing the location and strength of the heat source. We conducted simulations in the same manner as before, using only standard k–ε as the turbulence model. Figure **26** shows velocity distributions in the burning room from Code D using each of the three heat sources. Figure **27** does the same for results from Code C. The distributions from Code C are much smoother than those from Code D, regardless of the position of the heat source.

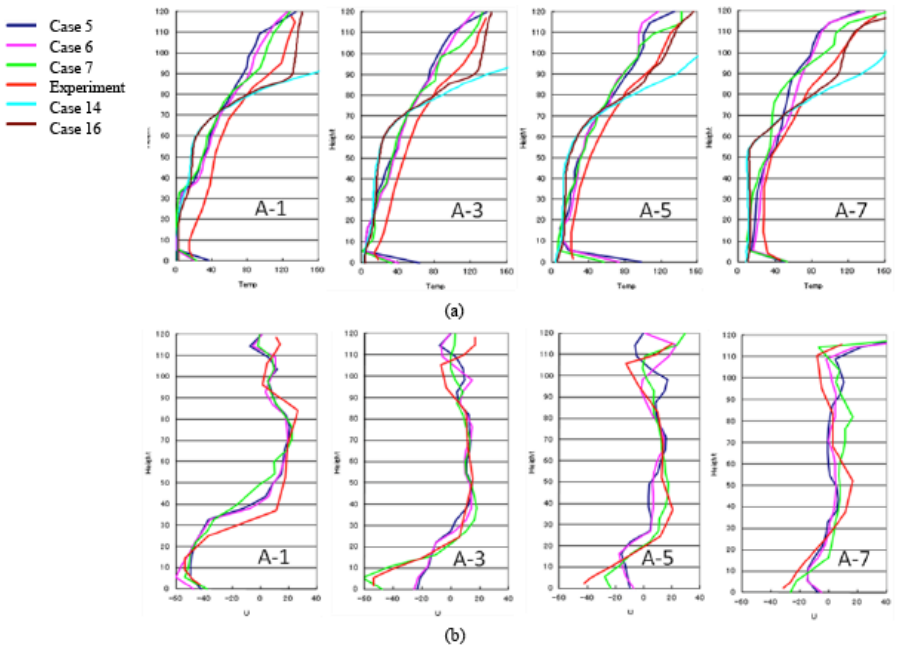

Figure 25: Profiles of (a) temperature and (b) velocity from experiment (red lines) and from simulations using different computational codes and turbulence models. Case 5 (blue lines): Code D, standard k–ε.

Case 6 (pink lines): code D, low-Re k–ε. Case 7 (green lines): Code D, RNG k–ε. Case 14 (aqua lines): Code C, standard k–ε. Case 16 (brown lines): Code C, RNG k–ε.

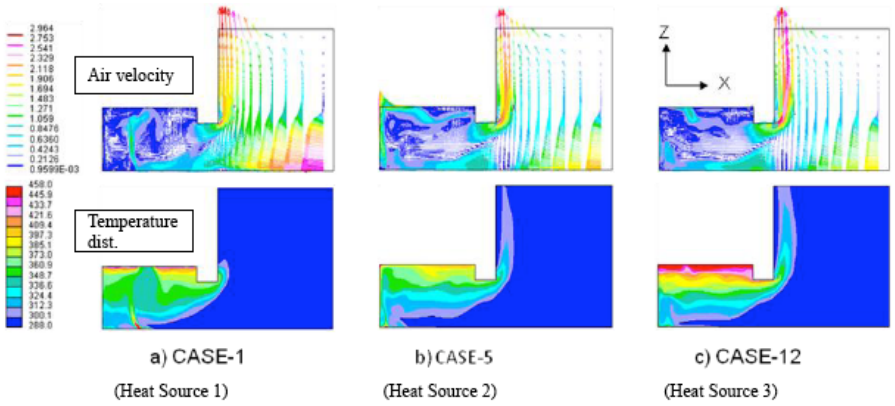

Figure 26: Differences in simulation results for air speed distributions from code D due to changes in location and intensity of the heat source. (a) Case 1 with heat source 1 in Figure **20**. (b) Case 5 with heat source 2. (c) Case 12 with heat source 3.

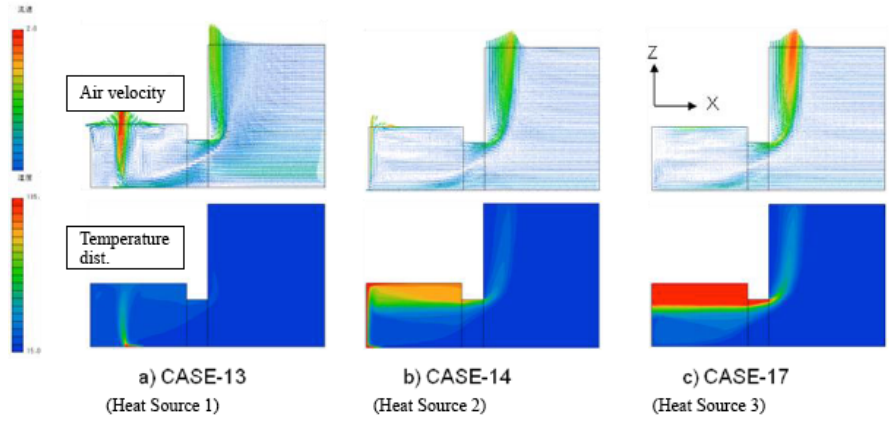

Figure 27: Differences in simulation results for air speed distributions from Code C due to changes in location and intensity of the heat source. (a) Case 13 with heat source 1 in Figure **20** (b) Case 14 with heat source 2. (c) Case 17 with heat source 3.

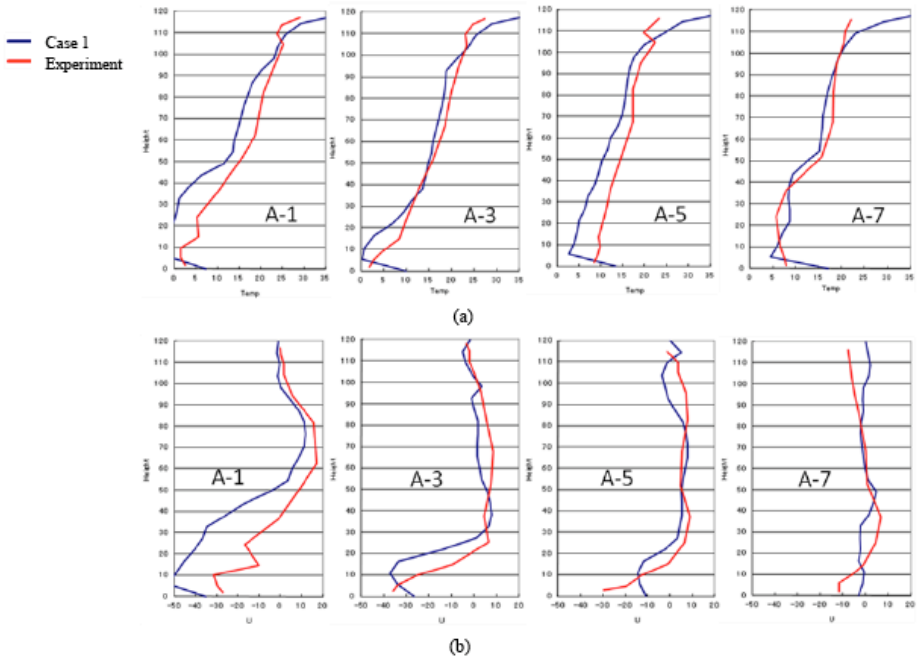

Figure 28: Simulation results for profiles of (a) temperature and (b) velocity from Case 1: Code D with the heat source 1 in Figure **20**.

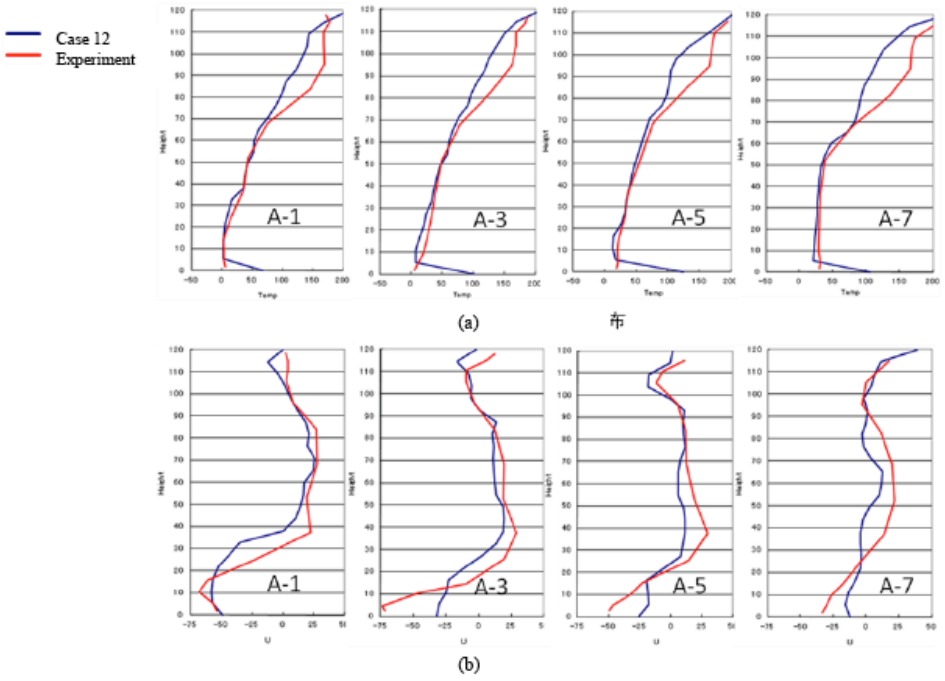

Figure 29: Simulation results for profiles of (a) temperature and (b) velocity from Case 12: Code D with heat source 3 in Figure **20**.

Figures **28** and **29** contain temperature and velocity profiles using Code D with heat source 1 (Figure **28**) and heat source 3 (Figure **29**). Although the simulations generally replicate the experimental results, there are some differences. In particular, when using heat source 1 (Figure **28**), there are significant differences in temperature distributions at the back of the burning room.

4.4.4. Differences Based on Whether or not Radiation was Included

Distributions in the burning room from simulations that did not take radiation heat transfer into consideration are given in Figure **30**. Results for vertical temperatures and air speeds from simulations that (1) included radiation analysis and (2) neglected radiation effect are compared in Figure **31**. When

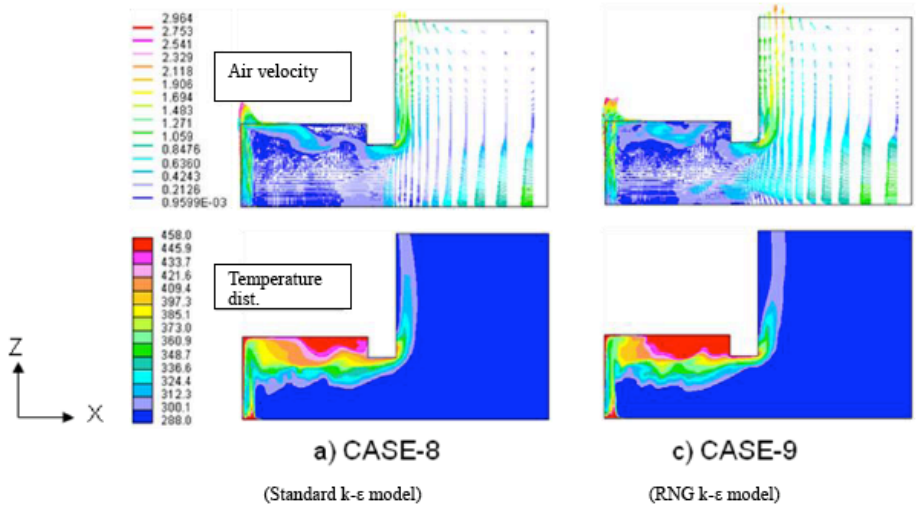

Figure 30: Simulation results for air speed distributions from code D in which radiation effects were neglected. In both cases, the heat source 2 was used. (a) Case 8 used the standard k–ε turbulence model. (b) Case 9 used the RNG k–ε turbulence model.

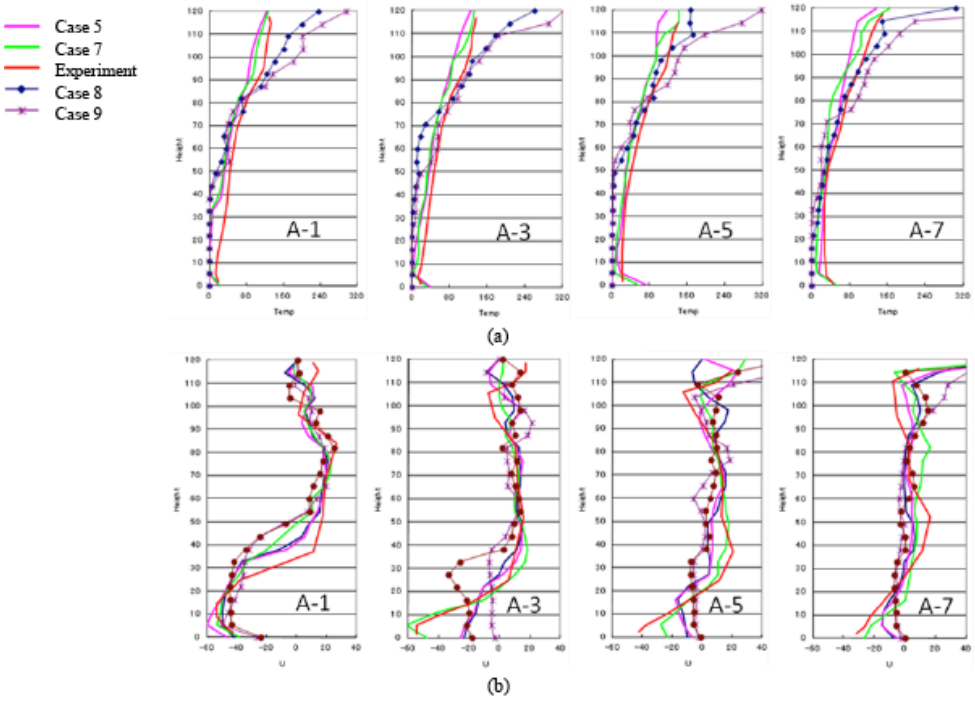

Figure 31: Simulation results for vertical distributions of (a) temperature and (b) air speed in which radiation effects were neglected (Cases 8 and 9, lines with points) compared with those in which radiation effects were included (Cases 5 and 7, lines without points).

radiation was neglected, the results show large increases in temperature near the ceiling of the burning room. This suggests that radiation interferes with the distribution of heat on high-temperature surfaces. The same trends also appear in Figure **31**. When radiation was neglected, temperatures near the ceiling were approximately double the values than those obtained when radiation was considered. In addition, when the RNG k–ε model was used and radiation was considered, it was relatively easy to reproduce the experimental air speed distribution near the floor. However, the ability to reproduce this distribution decreased substantially when radiation was neglected.

4.3.5. Differences Based on Compressible or Incompressible Air

All simulations discussed up to this point have assumed air is an incompressible viscous fluid with buoyancy effects included *via* the Boussinesq approximation. It has generally been thought that the Boussinesq approximation could not be used with large changes in temperature, like those in fires, so in such

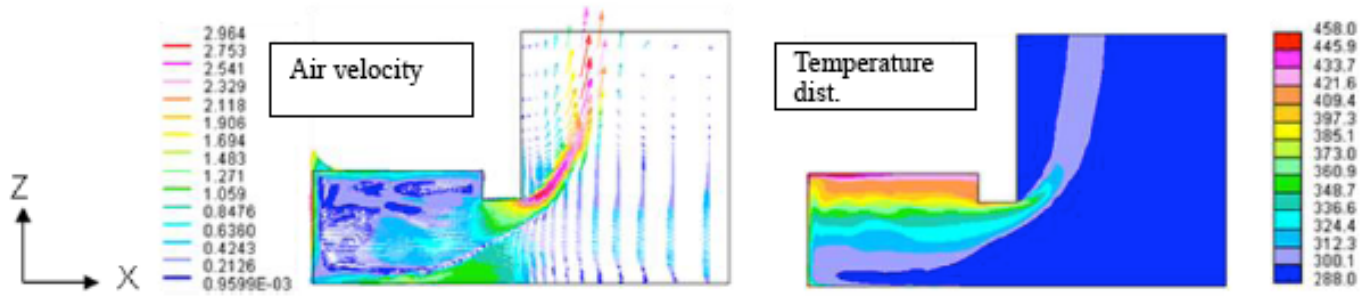

Figure 32: Simulation results for air speed distributions in which air was assumed to be compressible. Case 10: Code D, standard k–ε model, heat source 2, radiation included.

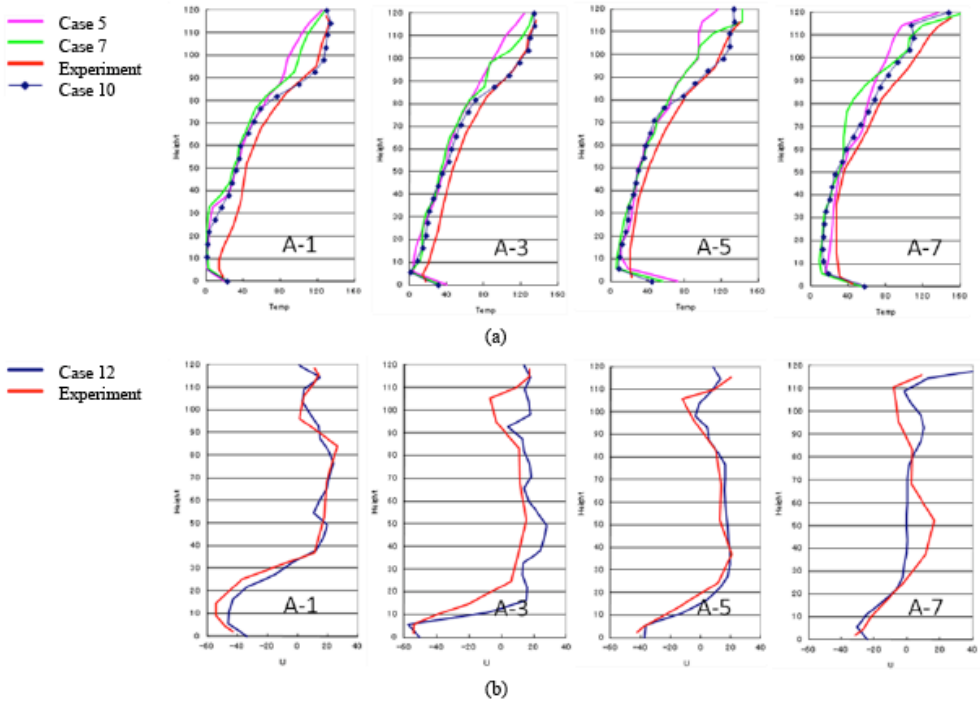

Figure 33: Profiles of (a) temperature and (b) velocity using Code D, heat source 2, radiation included, assuming air is compressible (Case 10, standard k–ε model) compared with results assuming air is incompressible (Case 5, standard k–ε model; Case 7, RNG k–ε model).

cases it is better to use compressible fluids. To test this, we conducted simulations in which air was assumed to be compressible. The results are displayed in Figures **32** and **33**.

Figure **32** contains results assuming a compressible fluid, where high-temperature air is pushed toward the outside of the hypothetical surrounding room. Using the Boussinesq approximation with the differences in temperature, we obtained linear increases in buoyancy. For comparison, we used an equation of state to compute the density distribution under the assumption that air is compressible. As a result, given that we were able to reproduce the buoyancy effect, the relationship between differences in temperature and buoyancy is not always linear. When the temperature differences are large, this will be especially true. So, it may be that this explains the differences found in the high-temperature airflows in the hypothetical surrounding rooms.

In Figure **33** the temperature and airflow velocity fields in the burning room for compressible air produce much closer agreement with experiment than those obtained assuming air is incompressible. In particular, distributions of temperature and speed near the ceiling and floor closely resemble those found in the experiment.

4.3.6. Differences Due to Changes in Methods Used to Set Exothermal Conditions

In the simulations described so far, exothermal conditions were set by putting a heat flux on the heating surface. Many simulation studies have been

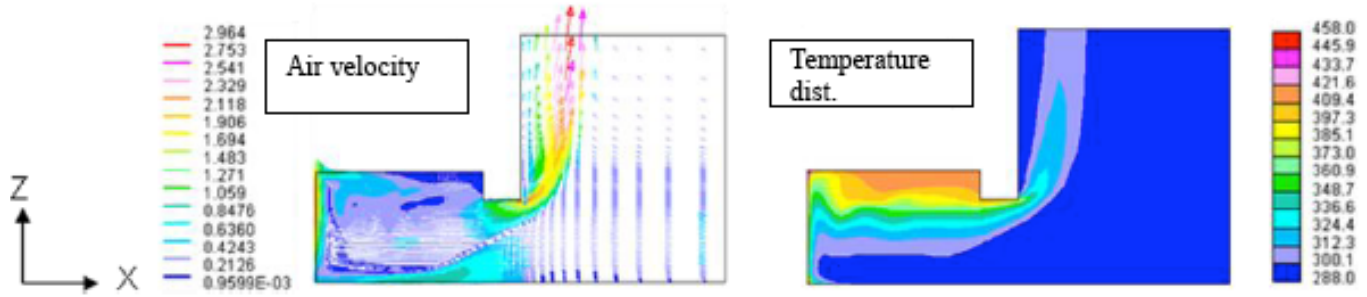

Figure 34: Two-dimensional air speed distributions from the burning room into an adjacent room from a simulation using fixed temperatures on the exothermal surface. Case 11: Code D, low-Re k–ε model, heat source 2, radiation included, air incompressible.

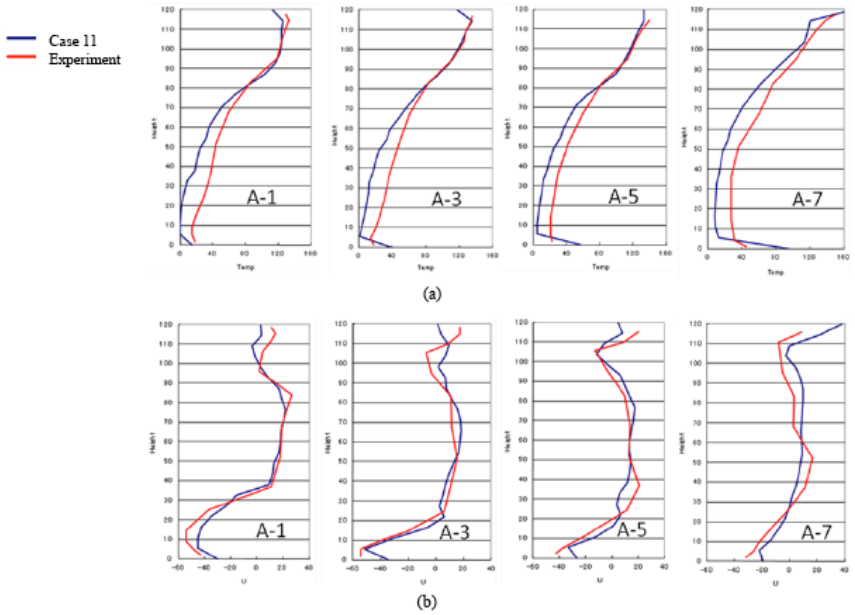

Figure 35: Temperature and velocity profiles from a simulation using fixed temperatures on the exothermal surface. Case 11: Code D, low-Re k–ε model, heat source 2, radiation included, air incompressible.

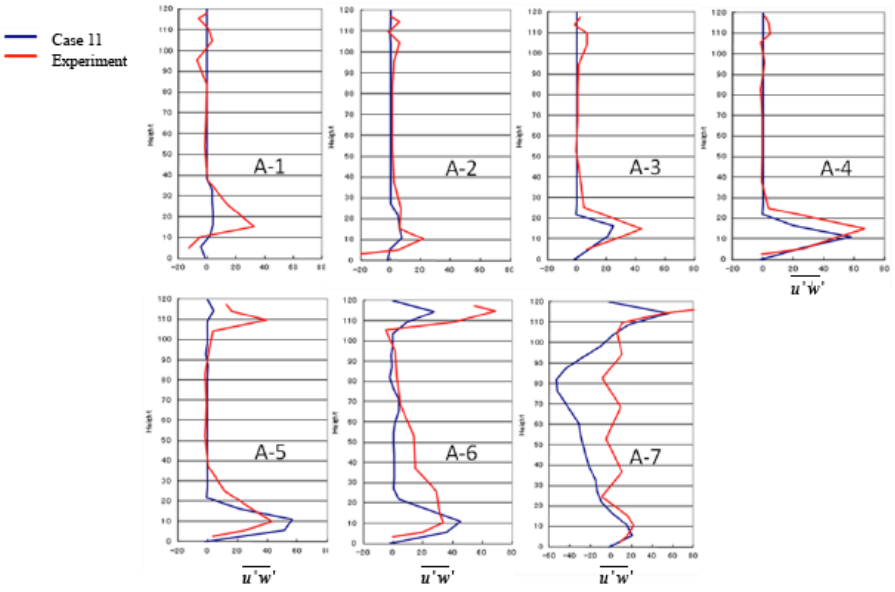

Figure 36: Comparisons of vertical distributions of Reynolds stress (cm^2/s^2) from experiment and from simulation using fixed temperatures on the exothermal surface (Case 11, as described in Figure **35**).

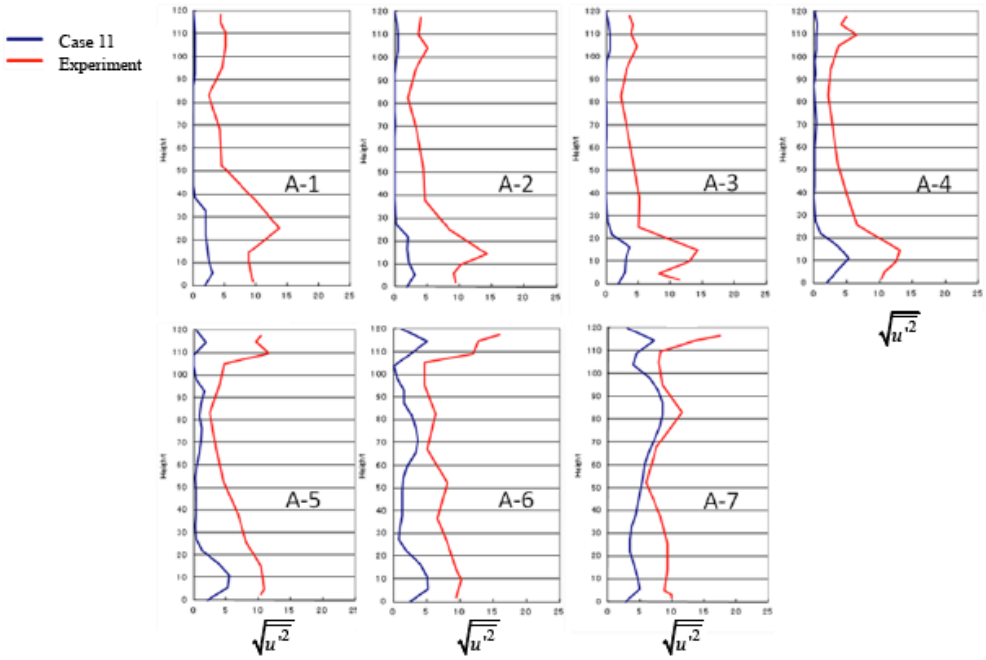

Figure 37: Simulation and experimental results for vertical distributions of RMS fluctuations (cm/s) in *x*-directional airflow. Simulations performed using fixed temperatures on the exothermal surface.

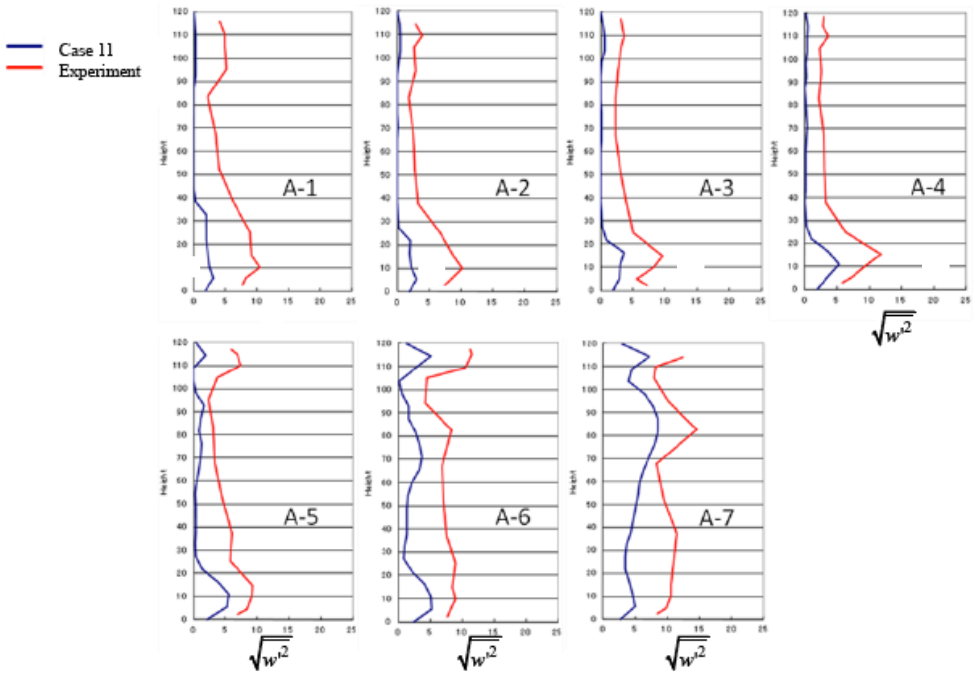

Figure 38: Simulation and experimental results for vertical distributions of rms fluctuations in *z*-directional airflow. Simulations performed using fixed temperatures on the exothermal surface.

performed using such settings. However, in their experiments, Murakami *et al*. [10] measured the temperatures across the exothermal surface in great detail. We used this data to create a simulation in which surface temperatures over the exothermal surface were fixed at the corresponding experimental values. Then we compared the average temperatures and average air speeds from the simulation to experimental values. The results can be found in Figures **34**–**37**.

Figure **34** shows results from simulations that used fixed temperatures on the exothermal surface. These results are very similar to those in Figure **32**, which assumed air is compressible. Further, this simulation produced velocity and temperature distributions in the

burning room that most closely coincide with experimental values (Figure **35**). In particular, note in both Figures **32** and **34** that the high-temperature air flowing into the hypothetical surrounding room does not adhere to wall surfaces.

Simulation results for the Reynolds stress distribution are compared with experimental data in Figure **36**. The simulation reproduced the peak that appears approximately 10 cm above the floor. However, differences occur between the experimental and simulated values near the ceiling and near the middle at measurement lines A6 and A7, which are near the aperture.

Simulation and experimental results of RMS fluctuations of airflows in the *x*- and *z*-directions are compared in Figures **37** and **38**, respectively. Although the distributions from simulation reproduce general characteristics of the experimental data, the simulations exhibit absolute values that are considerably lower than the experimental ones.

4.4. Discussions and Conclusions

We performed simulations under 17 different conditions to analyze fire-induced airflows; the simulation results were compared with experimental data. Phenomena in the burning room were most closely reproduced in three simulations: (a) Case 10 (simulation assuming air is compressible), (b) Case 11 (simulation in which air was assumed incompressible and exothermal surface temperatures were fixed at experimental values), and (c) Case 7 (simulation in which air was assumed incompressible and the RNG k–ε model was used as the turbulence model). These three cases included radiation effects, and the calculations stabilized after setting limitations on the ranges of outflow boundaries and free (unrestricted) airflows within the surrounding hypothetical room.

Generally differences between simulations were caused by the high-temperature airflows that entered the hypothetical surrounding room from the burning room. Both Cases 10 and 11 accurately reproduced the phenomena in the burning room, and both produced high-temperature airflows that were strongly pushed away from walls in the surrounding room. However, results for all other cases, including those implementing the Boussinesq approximation, showed high-temperature airflows adhering to the walls of surrounding rooms. We believe overestimations of buoyancy, which produced large differences in temperature, were due to the linear Boussinesq approximation. However, real fires that can flame through windows are known to spread to surrounding walls, then move upwards and continue to spread to upper floors. Based on the objectives of these simulations, we conclude that the overestimations of buoyancy due to the Boussinesq approximation were effective.

NOTES

CFD software in conducting benchmark tests.

(1) Code A: ANSYS/FLUENT®

(2) Code B: ANSYS/CFX®

(3) Code C: CRADLE/STREAM®

(4) Code D: IDAJ/STAR-CD®

(5) Code E: CRADLE/SCRYU Tetra®

(6) Code F: IDAJ/ STAR-CCM+®

(7) Code G: Open FOAM®

(8) Code H: Advanced Knowledge Laboratory/ Flow Designer®

REFERENCES

[1] Ito K, Inthavong K, Kurabuchi T, Ueda T, Endo T, Omori T, *et al*. Benchmark Tests Associated with Applying CFD to Indoor Environmental Problems: Part 1 Benchmark test for isothermal/non-isothermal flow in 2D and 3D room model. Int J Archit Eng Technol 2015; 2(1): 50-71.

[2] Ito K, Inthavong K, Kurabuchi T, Ueda T, Endo T, Omori T, *et al*. Benchmark Tests Associated with Applying CFD to Indoor Environmental Problems: Part 2 Benchmark test for cross-ventilation airflows and floor heating systems. Int J Archit Eng Technol 2015; 2(1): 72-48.

[3] Ito K, Inthavong K, Kurabuchi T, Ueda T, Endo T, Omori T, *et al*. Benchmark Tests Associated with Applying CFD to Indoor Environmental Problems: Part 3 Benchmark test for numerical thermal manikins. Int J Archit Eng Technol 2015; 2(1): 99-124.

[4] Momoi Y, Yamanaka T, Kotani H, Okaichi A. CFD of Airflows in Rooms with Anemostat Type: Part 5. CFD Simulation Using Measured Values of Velocity and Turbulence Parameters in Large Space as Boundary Conditions. Summaries of Technical Papers of Annual Meeting Architectural Institute of Japan 2001; 9: 775-776.

[5] Ueda T, Tatenooka M, Murakami Y. The Simple Approximation of Anemostat-type Air diffusers in CFD Simulation: Part 3. Comparison with the Experiment. Technical papers of annual meeting of the Society of Heating, Air-Conditioning and Sanitary Engineers of Japan, (In Japanese) 2010; 9: 2339-2342.

[6] Kondo Y, Akabayashi S, Kawase T, Ogata K, Yoshioka T. Study on Air-Conditioning, Ventilation System of Kitchen. : Part 7 Numerical Simulations of Flow and Temperature Distributions. Technical papers of annual meeting, the

Society of Heating, Air-Conditioning and Sanitary Engineers of Japan (In Japanese) 1994; C-17: 201-204.

[7] Kondo Y, Abe Y, Miyafuji A, Aizawa Y, Akagi K. CFD Modeling of Thermal Plume over a Cooking Pot and Experiments under Heating Condition, Indoor Temperature and Air Distributions of House Kitchens and Adjacent Living Rooms (Part 2). Architectural Institute of Japan, (In Japanese) 2008; 634: 1383-1390.

[8] Momose T, Yamanaka T, Kotani H, Yamamoto A. Measurement and Modeling of Plume abobe Commercial Cooking Stoves. Architectural Institute of Japan, (In Japanese) 2003; 567: 49-56.

[9] Kato S, Murakami S, Yoshie R. Experimental and Numerical Study on Natural Convection with Strong Density Variation along a Heated Vertical Plate, in 9th Symposium on Turbulent Shear Flows, 1993; 12-15.

[10] Murakami S, Kato S, Yoshie R. Measurement of Turbulence Statistics in a Model Fire Room by LDV. ASHRAE Transactions, 1995; 101:287-301.

Received on 03-12-2014 Accepted on 18-12-2014 Published on 07-04-2015

DOI: http://dx.doi.org/10.15377/2409-9821.2015.02.01.4